

The RNA-binding ubiquitin ligase MKRN1 functions in ribosome-associated quality control of poly(A)-translation

Andrea Hildebrandt¹, Mirko Brüggemann², Susan Boerner², Cornelia Rücklé², Jan Bernhard Heidelberg¹, Annabelle Dold¹, Anke Busch¹, Heike Hänel¹, Andrea Voigt¹, Stefanie Ebersberger¹, Ingo Ebersberger^{3,4}, Jean-Yves Roignant¹, Kathi Zarnack^{2§}, Julian König^{1§}, Petra Beli^{1§}

¹ Institute of Molecular Biology (IMB), Ackermannweg 4, 55128 Mainz, Germany

² Buchmann Institute of Molecular Life Sciences (BMLS), Goethe University, Max-von-Laue-Str. 15, 60438 Frankfurt am Main, Germany

³ Department for Applied Bioinformatics, Institute of Cell Biology and Neuroscience, Goethe University, Max-von-Laue-Str. 13, 60438 Frankfurt am Main, Germany

⁴ Senckenberg Biodiversity and Climate Research Centre (BiK-F), Georg-Voigt-Straße 14-16, 60325 Frankfurt am Main, Germany

§ Corresponding authors:

KZ (kathi.zarnack@bmls.de), JK (j.koenig@imb-mainz.de) and PB (p.beli@imb-mainz.de)

1 **Abstract**

2 Cells have evolved quality control mechanisms to ensure protein homeostasis by
3 detecting and degrading aberrant mRNAs and proteins. A common source of aberrant
4 mRNAs is premature polyadenylation, which can result in non-functional protein
5 products. Translating ribosomes encountering poly(A) sequences are terminally
6 stalled, followed by ribosome recycling and decay of the truncated nascent polypeptide
7 via the ribosome-associated quality control (RQC). Here, we demonstrate that the
8 conserved RNA-binding E3 ubiquitin ligase Makorin Ring Finger Protein 1 (MKRN1)
9 promotes ribosome stalling at poly(A) sequences during RQC. We show that MKRN1
10 is positioned upstream of A-rich stretches and poly(A) tails in mRNAs through an
11 interaction with the cytoplasmic poly(A)-binding protein (PABP). We uncover PABP,
12 ribosomal protein RPS10, and additional translational regulators as main ubiquitylation
13 substrates of MKRN1. Consequently, we propose that MKRN1 serves as a first line of
14 poly(A) recognition at the mRNA level to prevent production of erroneous proteins, thus
15 maintaining proteome integrity.

16 **Keywords**

17 MKRN1, ubiquitylation, RNA binding, ribosome-associated quality control, RQC,

18 poly(A), iCLIP, ubiquitin remnant profiling, translation

19 **Introduction**

20 During gene expression, quality control pathways monitor each step to detect aberrant
21 mRNAs and proteins. These mechanisms ensure protein homeostasis and are
22 essential to prevent neurodegenerative diseases (Chu et al. 2009). A common source
23 of aberrant mRNAs is premature polyadenylation, often in combination with mis-
24 splicing, which results in truncated non-functional protein products (Kaida et al. 2010).
25 Therefore, mechanisms are in place that recognise such homopolymeric adenosine
26 (poly(A)) sequences and abrogate their translation (Bengtson and Joazeiro 2010).

27 In eukaryotes, ribosomes that terminally stall for diverse reasons during translation are
28 detected by the ribosome-associated quality control (RQC) (reviewed in Brandman and
29 Hegde 2016; Joazeiro 2017). Upon splitting of the 60S and 40S ribosomal subunits,
30 the RQC complex assembles on the stalled 60S subunit to initiate the release and
31 rapid degradation of the truncated tRNA-bound polypeptide. The E3 ubiquitin ligase
32 Listerin (LTN1) modifies the truncated polypeptide with K48-linked ubiquitin chains to
33 target it for degradation in a p97-dependent manner through the proteasome
34 (Bengtson and Joazeiro 2010; Brandman et al. 2012; Verma et al. 2013). Whereas
35 peptide release and ribosome recycling by the RQC complex are relatively well
36 understood, less is known about the mechanisms that promote poly(A) recognition and
37 initial ribosome stalling.

38 Several recent studies demonstrated a role for the RNA-binding E3 ubiquitin ligase
39 ZNF598 in initiating RQC for prematurely polyadenylated mRNAs (Garzia et al. 2017;
40 Juskiewicz and Hegde 2017; Sundaramoorthy et al. 2017). It was suggested that
41 ZNF598 senses the translation of poly(A) segments through binding the cognate lysine
42 tRNAs (Garzia et al. 2017). In addition, ZNF598 recognises the collided di-ribosome
43 structure that arises when a trailing ribosome encounters a slower leading ribosome

44 (Juszkiewicz et al. 2018). This is followed by site-specific, regulatory ubiquitylation of
45 the 40S ribosomal proteins RPS10 and RPS20 by ZNF598. In addition to ZNF598, the
46 40S ribosomal subunit-associated protein RACK1 was shown to regulate ubiquitylation
47 of RPS2 and RPS3 upstream of ribosomal rescue (Sundaramoorthy et al. 2017).

48 Makorin Ring Finger Protein 1 (MKRN1) belongs to a family of evolutionary conserved
49 RNA-binding E3 ubiquitin ligases. Up to four paralogs exist in vertebrates (MKRN1-4),
50 which combine a RING domain with one or more CCCH zinc finger domains (Gray et
51 al. 2000; Böhne et al. 2010) (**Supplemental Fig. 1A**). MKRN1 has been implicated in
52 the regulation of telomere length, RNA polymerase II transcription and the turnover of
53 tumour suppressor protein p53 and cell cycle regulator p21 (Kim et al. 2005;
54 Omwancha et al. 2006; Lee et al. 2009; Salvatico et al. 2010), but its RNA-related
55 functions remain poorly understood. A study in mouse embryonic stem cells (mESC)
56 reported its interaction with hundreds of mRNAs as well as multiple RNA-binding
57 proteins (RBPs), including the cytoplasmic poly(A)-binding protein (PABP) PABPC1,
58 IGF2BP1 and ELAVL1 (Cassar et al. 2015). The interaction with PABP was further
59 corroborated in human HEK293 cells (Miroci et al. 2012). The same study
60 demonstrated that a shortened isoform of MKRN1 controls local translation via its
61 PABP-interacting motif 2 (PAM2 motif) in rat neurons (Miroci et al. 2012).
62 Nevertheless, the RNA binding specificity and functional role of MKRN1 in human cells
63 remained largely elusive.

64 Here, we introduce MKRN1 as a novel factor in RQC. MKRN1 is recruited to A-rich
65 sequences in mRNAs in a PABP-dependent manner, where it acts as a first line of
66 defence against poly(A) translation. MKRN1 depletion abrogates ribosome stalling in
67 reporter assays, accompanied by reduced ubiquitylation of RQC-related proteins. We

- 68 propose that MKRN1 allows recognition of poly(A) sequences prior to their translation,
69 which may be particularly beneficial in humans.

70 **Results**

71 **MKRN1 forms an mRNP with PABPC1 and other RBPs**

72 In order to learn about potential functions, we first characterised the protein interaction
73 profile of MKRN1 in HEK293T cells. To this end, we used affinity purification (AP)
74 coupled to stable isotope labelling with amino acids in cell culture (SILAC)-based
75 quantitative mass spectrometry (MS) using GFP-MKRN1^{wt} or GFP as a bait. We
76 identified 53 proteins that were significantly enriched in GFP-MKRN1^{wt} compared to
77 the control APs (false discovery rate [FDR] < 5%, combined ratios of three independent
78 experiments). In line with previous reports (Miroci et al. 2012; Cassar et al. 2015;
79 Hildebrandt et al. 2017), we found the cytoplasmic poly(A)-binding proteins (PABP)
80 PABPC1 and PABPC4 among the highly enriched MKRN1 interactors (z-score > 4,
81 corrected *P* values = 7.18e-10 and 6.16e-16, respectively) (**Fig. 1A, Supplemental**
82 **Fig. S2A, and Supplemental Table S1**). Moreover, we detected 14 ribosomal proteins
83 as well as four proteins that were previously shown to co-purify with ribosomes (Simsek
84 et al. 2017), including IGF2BP1, LARP1, UPF1 and ELAVL1 (**Fig. 1A**). Consistently,
85 “translation” was among the significantly enriched Gene Ontology (GO) terms for the
86 MKRN1 interaction partners (Biological Process [BP], **Supplemental Fig. S2B**).
87 Almost all interactors were previously found in association with polyadenylated
88 transcripts (50 out of 53 proteins have been annotated with the GO term “poly(A) RNA
89 binding”, Molecular Function [MF], **Supplemental Fig. S2B**). We confirmed the MS
90 results in reciprocal AP experiments with GFP-tagged PABPC1, ELAVL1 and
91 IGF2BP1 as baits followed by Western blot for endogenous MKRN1 (**Supplemental**
92 **Fig. S2C**). All detected interactions persisted in the presence of RNases (RNase A
93 and T1), demonstrating that MKRN1 interacts with these proteins in an RNA-
94 independent manner (**Supplemental Fig. S2C**). Together, these observations suggest

95 that MKRN1 is part of a larger mRNA ribonucleoprotein particle (mRNP) together with
96 PABP and other RBPs. This is further supported by a parallel study with the Mkrn1
97 ortholog in *Drosophila melanogaster*, which consistently identified pAbp, Larp, Upf1
98 and Imp (IGF2BP in mammals) as interaction partners (Dold et al, parallel submission).
99 Many proteins interact with PABP via a PABP-interacting motif (PAM2) motif, which
100 specifically binds to the MLLE domain present almost exclusively in PABP (Deo et al.
101 2001; Kozlov et al. 2010). Accordingly, a previous study demonstrated that MKRN1
102 associates with PABP via a PAM2 motif at amino acid positions 161-193 (Miroci et al.
103 2012). In support of a putative functional relevance, the presence and positioning of
104 the PAM2 motif are preserved in MKRN1 orthologs across metazoans (**Supplemental**
105 **Fig. S1A,B**). AP of a MKRN1 variant with three point mutations in the PAM2 motif
106 (GFP-MKRN1^{PAM2mut}) (Pohlmann et al. 2015) no longer recovered PABPC1 and
107 PABPC4 (**Fig. 1B-D** and **Supplemental Table S1**). For comparison, we also tested a
108 previously described point mutation in the RING domain that abolishes the E3 ubiquitin
109 ligase function (ligase-dead, GFP-MKRN1^{RINGmut}) (Kim et al. 2005). This mutation did
110 not impair the interaction of MKRN1 with PABPC1, but rather led to a slight increase,
111 possibly due to stabilisation of MKRN1 and/or PABPC1 (**Fig. 1C** and **Supplemental**
112 **Table S1**). Surprisingly, MKRN1^{PAM2mut} lost interaction not only with PABPC1 and
113 PABPC4, but also with several other identified proteins (**Fig. 1D**), suggesting that
114 MKRN1^{PAM2mut} no longer resided within the mRNPs. These results demonstrate that
115 MKRN1 interacts with PABP proteins, which is required for mRNP formation.

116 **PABP recruits MKRN1 to bind upstream of A-stretches and poly(A) tails**

117 In order to characterise the RNA binding behaviour of human MKRN1 *in vivo*, we
118 performed individual-nucleotide resolution UV crosslinking and immunoprecipitation
119 (iCLIP) (König et al. 2010) in combination with 4-thiouridine labelling to enhance UV

120 crosslinking (Hafner et al. 2010). In three replicate experiments with GFP-tagged
121 MKRN1 (GFP-MKRN1^{wt}) expressed in HEK293T cells, we identified more than 4,6
122 million unique crosslink events, cumulating into 7,331 MKRN1 binding sites (see
123 Materials and methods; **Supplemental Table S2**). In order to estimate the strength of
124 MKRN1 binding, we normalised the crosslink events within each binding site to the
125 background in the surrounding sequence, which served as a proxy for the abundance
126 of the underlying transcript (“signal-over-background”, SOB; see Materials and
127 Methods) (Sutandy et al. 2018). SOB values were highly reproducible between
128 replicates (Pearson correlation coefficients $r > 0.72$, **Supplemental Fig. S3**). Based
129 on the SOB values, we stratified the MKRN1 binding sites into 20% quantiles of
130 increasing binding strength for further analysis.

131 Across the transcriptome, MKRN1 almost exclusively bound to protein-coding mRNAs
132 with a strong tendency to locate in 3' UTRs (**Fig. 2A,E**). Strikingly, the top 20% MKRN1
133 binding sites were characterised by a massive accumulation of AAAA (A, adenosine)
134 within 5-50 nucleotides (nt) downstream of the binding sites (**Fig. 2B** and
135 **Supplemental Fig. S4A**). In addition, we found an enrichment of uridine-rich tetramers
136 within MKRN1 binding sites (**Fig. 2B**), which likely arises from 4SU-based UV
137 crosslinking (Hafner et al. 2010).

138 In order to characterise the RNA sequence preference in more detail, we retrieved the
139 associated A-rich stretches (A-stretches) downstream of MKRN1 binding sites based
140 on the overall A-content and the longest continuous A-tract (see Materials and
141 methods). The identified A-stretches ranged from 8-30 nt in length (**Supplemental Fig.**
142 **S4B**). Within 3' UTRs, 30% (1,848 out of 6,165) of MKRN1 binding sites resided next
143 to an A-stretch, and MKRN1 binding peaked immediately upstream (**Fig. 2C,E**).
144 Overlaying the A-stretches with MKRN1 binding strength, we found that longer A-

145 stretches associated with stronger MKRN1 binding, which plateaued from 25-nt A-
146 stretches onwards (mean SOB; **Supplemental Fig. S4C,D**). We also detected a
147 requirement for a continuous run of at least 8 A's to confer strong MKRN1 binding (**Fig.**
148 **2D**). Intriguingly, these observations precisely matched the previously reported RNA
149 binding preferences of PABP (Webster et al. 2018), indicating that MKRN1 binds
150 together with PABP to mRNAs.

151 Prompted by this notion, we searched for iCLIP reads that may originate from poly(A)
152 tails and are hence challenging to map to the genome. We found an unusually high
153 fraction of unmapped reads (41%) in the MKRN1 iCLIP datasets (**Supplemental Table**
154 **S2**). More than 13% of these unmapped reads displayed an increased A-content (**Fig.**
155 **3B**), compared to only 2% for an unrelated control RBP (Braun et al. 2018), suggesting
156 that they could indeed reflect immediate MKRN1 binding on poly(A) tails. In addition,
157 we found that GFP-MKRN1^{wt} crosslink events were enriched upstream of annotated
158 transcript 3' ends (**Fig. 2E** and **Fig. 3A,C**). Together, these results indicate that, in
159 addition to the internal A-stretches within 3' UTRs, MKRN1 shows binding at poly(A)
160 tails. This binding behaviour is illustrated in the *SRSF4* gene, which displays
161 pronounced MKRN1 binding upstream of the annotated 3' end (**Fig. 3A**).

162 Based on the strong interaction with PABP (**Fig. 1A,C**), we hypothesised that PABP
163 might recruit MKRN1 to the A-stretches and poly(A) tails. In order to test this, we
164 performed UV crosslinking experiments with GFP-MKRN1^{PAM2mut}, which no longer
165 interacts with PABP (**Fig. 1C,D**). Strikingly, RNA binding of this mutant was globally
166 reduced compared to GFP-MKRN1^{wt} (**Fig. 3D** and **Supplemental Fig. S5**). In
167 summary, these results imply that MKRN1 is positioned by PABP in front of A-stretches
168 in 3' UTRs and poly(A) tails.

169 **MKRN1 promotes ribosome stalling at poly(A) sequences**

170 Based on MKRN1's association with poly(A) tails as well as its interaction with PABP
171 and ribosomal proteins, we hypothesised that MKRN1 may be involved in ribosome-
172 associated quality control (RQC). In this process, ribosomes that translate into a
173 poly(A) sequence, for instance upon stop codon readthrough and premature
174 polyadenylation, are stalled and eventually recycled (Brandman and Hegde 2016;
175 Joazeiro 2017). To test this hypothesis, we employed a recently introduced flow
176 cytometry-based assay that monitors ribosome stalling in a dual fluorescence reporter
177 (Juszkiewicz and Hegde 2017) (**Fig. 4A**).

178 As reported previously, inserting a K(AAA)₂₀ linker (encoding for 20 lysine residues)
179 into the reporter resulted in predominant ribosome stalling compared to the starting
180 vector (K₀, **Fig. 4B** and **Supplemental Fig. 6A**). Importantly, *MKRN1* depletion with
181 two independent siRNA sequences led to a reproducible recovery of RFP expression
182 downstream of K(AAA)₂₀, demonstrating that ribosomes failed to stall at K(AAA)₂₀
183 (*MKRN1* KD1 and KD2; **Fig. 4C** and **Supplemental Fig. S6A,B**). *MKRN1* KD2
184 seemed slightly more effective, possibly because this siRNA simultaneously
185 decreased the transcript levels of the close paralogue *MKRN2* (**Supplemental Fig.**
186 **S6C**). Notably, *MKRN1* KD2 impaired ribosome stalling to a similar level as KD of
187 *ZNF598*, the E3 ubiquitin ligase that was recently reported to function in RQC (Garzia
188 et al. 2017; Juszkiewicz and Hegde 2017; Sundaramoorthy et al. 2017). Simultaneous
189 depletion of *MKRN1* and *ZNF598* was not additive, indicating that both proteins are
190 necessary for function (**Fig. 4C** and **Supplemental Fig. S6A**). However, we noted a
191 certain level of cross-regulation, such that *ZNF598* expression was decreased in
192 *MKRN1* KD1 (but not in *MKRN1* KD2), whereas *ZNF598* overexpression reduced
193 *MKRN1* expression (**Supplemental Fig. S6D,E**). Taken together, we conclude that
194 MKRN1 is required for efficient ribosome stalling in RQC.

195 **MKRN1 mediates the ubiquitylation of ribosome-associated proteins**

196 In order to identify putative ubiquitylation substrates of MKRN1, we determined the
197 protein interactome of the ligase-deficient mutant GFP-MKRN1^{RINGmut}. In three
198 replicate experiments, we quantified 1,097 protein groups present in at least two out
199 of three replicates (**Supplemental Table S1**), revealing 137 proteins that were
200 significantly enriched compared to GFP-MKRN1^{wt} (**Supplemental Fig. S7**).
201 Intriguingly, these candidates for ubiquitylation included RPS10, a ribosomal protein
202 that was reported to be modified by ZNF598 during RQC (Garzia et al. 2017;
203 Juskiewicz and Hegde 2017; Sundaramoorthy et al. 2017).

204 In order to directly test for ubiquitylation of putative substrates of MKRN1, we
205 performed ubiquitin remnant profiling to compare the relative abundance of di-glycine-
206 modified lysines in wild type and *MKRN1* KD cells. We quantified a total of 15,528
207 ubiquitylation sites on 4,790 proteins, out of which 2,324 ubiquitylation sites (in 1,264
208 proteins) were detected in all four replicate experiments (**Supplemental Table S3**).
209 Notably, *MKRN1* depletion led to a significantly decreased abundance of 29
210 ubiquitylation sites on 21 proteins (FDR < 10%, **Fig. 5A**). The majority of the
211 ubiquitylation targets assembled into a coherent cluster of translational regulators
212 based on previously reported protein-protein interactions and functional annotations
213 (**Fig. 5B,C** and **Supplemental Fig. 8A**). Among these proteins, we had already
214 detected PABPC1/4, IGF2BP1, ELAVL1, MOV10, LARP1 and RPS10 as significant
215 interactors of GFP-MKRN1^{wt} and/or GFP-MKRN1^{RINGmut} (**Fig. 1A**, **Fig. 5F** and
216 **Supplemental Fig. S7**). Importantly, we detected a significant decrease in
217 ubiquitylation at lysine 107 of RPS10 (K107; **Fig. 5D**). In order to distinguish differential
218 ubiquitylation from protein level changes, we also measured the total protein levels in
219 *MKRN1* KD cells and did not observe changes in RPS10, PABPC1/4, IGF2BP1/2/3,

220 ELAVL1, and MOV10 protein levels (**Supplemental Fig. 8B** and **Supplemental Table**
221 **S4**). This result further supported the notion that these proteins are ubiquitylated by
222 MKRN1. Taken together, we conclude that MKRN1 mediates ubiquitylation of the
223 ribosomal protein RPS10 and several translational regulators during ribosome-
224 associated quality control.

225 **Discussion**

226 Ribosome-associated quality control is essential to recognise and clear terminally
227 stalled ribosomes. Here, we uncover MKRN1 as a novel sensor for poly(A) sequences
228 in RQC. Our data indicate that MKRN1 is positioned upstream of poly(A) sequences
229 through direct interaction with PABP, thereby marking the beginning of poly(A) tails.
230 We propose that in case of premature polyadenylation, MKRN1 stalls the translating
231 ribosome and initiates RQC by ubiquitylating ribosomal protein RPS10, PABP and
232 other translational regulators (**Fig. 6**).

233 **PABP recruits MKRN1 upstream of A-stretches and poly(A) tails**

234 Central to our model is the specific RNA binding behaviour of MKRN1, which is
235 recruited to mRNA by PABP to mark internal A-stretches and the beginning of poly(A)
236 tails. This builds on the following observations: (i) We and others show that MKRN1
237 and PABP interact via the PAM2 motif (Miroci et al. 2012). (ii) We observe the strongest
238 MKRN1 binding sites upstream of A-stretches in the 3' UTR, where it likely coincides
239 with PABP binding (Bag 2001; Lyabin et al. 2011). (iii) MKRN1 binding to RNA is
240 strongly reduced when interaction with PABP is abolished. (iv) The association of
241 strong MKRN1 binding with continuous A-runs of ≥ 8 A's mirrors the footprint of one
242 RNA recognition motif (RRM) domain of PABP, indicating that one RRM binding to
243 poly(A) is sufficient for MKRN1 recruitment (Webster et al. 2018). On such short A-
244 stretches, MKRN1 might stabilise PABP binding, while on longer A-stretches, PABP
245 might be the major driving force to recruit MKRN1. This interaction might also anchor
246 the first PABP at the beginning of the poly(A) tail. One possible function could be the
247 stabilisation of PABP on short poly(A) tails to promote efficient translation (Lima et al.
248 2017). In yeast, where a MKRN1 ortholog is missing (see below), this anchoring is
249 thought to be achieved by Pab1p itself via its fourth RRM domain (Webster et al. 2018).

250 Of note, a parallel study with the Mkrn1 ortholog from *D. melanogaster* demonstrates
251 binding of a Mkrn1/pAbp complex at an A-stretch in the 3' UTR of *oskar* mRNA, which
252 is involved in translational control and required for oogenesis (Dold et al., parallel
253 submission).

254 **MKRN1 ubiquitylates RPS10 and translational regulators to stall ribosomes**

255 Our data suggest that ribosomes encountering the MKRN1-PABP complex at poly(A)
256 tails are stalled via ubiquitylation of RPS10 and other MKRN1 interactors. This is
257 supported by previous reports on ubiquitylation of ribosomal proteins, including
258 RPS10, which results in ribosome stalling e.g. during the unfolded protein response
259 (Higgins et al. 2015). ZNF598 and RACK1, the two factors that were recently shown
260 to function in RQC of poly(A) translation, were also found to mediate ubiquitylation of
261 these ribosomal proteins (Juszkiewicz et al. 2018). We hypothesise that MKRN1 is
262 specifically involved in preventing the translation of (premature) poly(A) tails. MKRN1
263 is recruited by PABP to the beginning of poly(A) tails, where it represents a physical
264 "roadblock" to the translating ribosome. We propose that upon contact with the
265 translating ribosome, MKRN1 ubiquitylates K107 on RPS10, thereby stalling the
266 ribosome before it translates the poly(A) tail. Subsequently, the trailing ribosomes
267 collide with the initially stalled ribosome. ZNF598 recognises the collision interface and
268 ubiquitylates the collided ribosomes (Simms et al. 2017; Juszkiewicz et al. 2018). In
269 summary, we propose that a sequence of MKRN1-mediated and ZNF598-mediated
270 ubiquitylation events on ribosomal proteins and possibly other factors, including
271 PABPC1, triggers ribosome-associated quality control.

272 **Differences between human and yeast RQC explain requirement for MKRN1**

273 Many known components of the RQC machinery, such as listerin (Ltn1p in yeast) and
274 ZNF598 (Hel2p in yeast), are identical from yeast to human, however the molecular

275 signals that are recognised differ partially. In yeast, RQC can be triggered by an excess
276 of positively charged amino acids (lysine and arginine), which are sensed while they
277 pass through the ribosomal exit tunnel (Lu and Deutsch 2008; Letzring et al. 2013). In
278 contrast, in human, sensing the aberrant mRNAs does not occur via the encoded
279 amino acids but at the level of the mRNA sequence and corresponding tRNAs, such
280 that only poly(A) effectively results in ribosome stalling (Arthur et al. 2015; Garzia et al.
281 2017; Juskiewicz and Hegde 2017). We propose that MKRN1 acts as direct reader
282 of poly(A) sequences based on its interaction with PABP. Consistent with this
283 conceptual difference, there is no functionally equivalent ortholog of MKRN1 in yeast
284 (Yth1p and Lee1p are similar, but lack RING domain and PAM2 motif; **Supplemental**
285 **Fig. 1C**). Why yeast and human employ partially different mechanisms to detect
286 poly(A) translation is currently unclear, but it has been suggested that spurious
287 translation of poly-lysine stretches from long human poly(A) tails might target the
288 aberrant proteins to the nucleus (Juskiewicz and Hegde 2017). Loss of mRNA
289 surveillance and RQC deficiency can lead to protein aggregation and culminate in
290 proteotoxic stress, which in turn is linked to neurological disorders such as amyotrophic
291 lateral sclerosis (Choe et al. 2016; Jamar et al. 2018). Hence, recognition of poly(A)
292 sequences prior to their translation might be particularly beneficial in humans.

293 **Materials and methods**

294 **Cell culture**

295 HEK293T cells were obtained from DSMZ and cultured in DMEM (Life Technologies)
296 with 10% fetal bovine serum (Life Technologies), 1% penicillin/streptomycin (Life
297 Technologies), and 1% L-glutamine (Life Technologies). All cells were maintained at
298 37°C in a humidified incubator containing 5% CO₂ and routinely tested for mycoplasma
299 infection. For SILAC labelling, cells were maintained in media containing either L-
300 arginine and L-lysine (light SILAC label), L-arginine (¹³C₆) and L-lysine (²H₄) (medium
301 SILAC label), or L-arginine (¹³C₆-¹⁵N₄) and L-lysine (¹³C₆-¹⁵N₂) (heavy SILAC label)
302 (Cambridge Isotope Laboratories).

303 **Vectors**

304 The following vectors, suitable for Gateway Cloning, were obtained either from the IMB
305 Core Facility ORFeome Collection (Collaboration 2016) or from the Harvard PlasmID
306 Repository (<https://plasmid.med.harvard.edu/PLASMID/>): pENTR221-MKRN1,
307 pENTR221-PABPC1, pENTR223.1-IGF2BP1, pENTR221-ELAVL1, pCMV-SPORT-
308 ZNF598. Coding sequences from the entry vectors were cloned into the mammalian
309 expression vectors pMX-DEST53-IP-GFP by LR Gateway cloning according to the
310 manufacturer's recommendations (Gateway LR Clonase II Enzyme mix; Life
311 Technologies). Dual fluorescence reporter plasmids (pmGFP-P2A-K₀-P2A-RFP,
312 pmGFP-P2A-(K^{AAA})₁₂-P2A-RFP, pmGFP-P2A-(K^{AAA})₂₀-P2A-RFP, and pmGFP-P2A-
313 (R^{CGA})₁₀-P2A-RFP) were generously provided by Ramanujan S. Hegde (MRC
314 Laboratory of Molecular Biology, Cambridge, UK) (Juszkiewicz and Hegde 2017).

315 **Cloning**

316 All MKRN1 mutant plasmids were generated with the Q5 Site-Directed Mutagenesis
317 Kit (NEB) according to the manufacturer's recommendations. In order to disrupt

318 MKRN1's interaction with PABP (MKRN1^{PAM2mut}), three point mutations were
319 introduced into the PAM2 motif (A169S, F172A, P174A; **Fig. 1B**) as previously
320 described (Pohlmann et al. 2015). In MKRN1^{RINGmut}, a previously described mutation
321 in the RING domain (H307E) was introduced to abolish E3 ubiquitin ligase function
322 (Kim et al. 2005). All primers used for introducing mutations into MKRN1 are listed in
323 **Supplemental Table S5**.

324 **Transfections**

325 Overexpression of vectors was performed using Polyethylenimine MAX 4000
326 (Polysciences, 24885-2) with a DNA:PEI ratio of 1:10. Knockdowns were performed
327 with siRNAs (**Supplemental Table S6**) using Lipofectamine RNAiMAX (Life
328 Technologies) according to the manufacturer's recommendations.

329 **Affinity purification (AP) for Western blot analyses**

330 GFP-based affinity purifications (APs) were performed as described before
331 (Hildebrandt et al. 2017). In brief, HEK293T cells transiently expressing GFP (empty
332 vector) or a GFP-tagged target protein were used. The cells were lysed in modified
333 RIPA (mRIPA) buffer supplemented with protease inhibitors (protease inhibitor
334 cocktail, Sigma), 1 mM sodium orthovanadate, 5 mM β -glycerophosphate, 5 mM
335 sodium fluoride, and 10 mM N-ethylmaleimide (NEM) (all from Sigma). Protein
336 concentrations were determined using the Pierce BCA Protein Assay Kit (Thermo
337 Fisher). GFP-trap agarose beads (Chromotek) were incubated with the cleared lysate
338 for 1 h at 4°C. After five washes with mRIPA buffer, the beads were resuspended in
339 LDS sample buffer (Life Technologies) and heated to 70°C for 10 min. For RNase
340 digests, the enriched proteins were incubated with 0.5 U/ μ l RNase A (Qiagen) and
341 20 U/ μ l RNase T1 (Thermo Fisher Scientific) for 30 min at 4°C after the first two washes
342 in mRIPA buffer.

343 **Sample preparation for the protein interactome analysis**

344 GFP-based APs were performed as described before (Hildebrandt et al. 2017). In brief,
345 HEK293T cells transiently expressing GFP (empty vector) were cultured in light SILAC
346 medium, while cells expressing N-terminally GFP-tagged MKRN1 wt or mutants were
347 cultured in medium or heavy SILAC medium. The cells were lysed as described above.
348 After washing in mRIPA buffer, GFP-trap agarose beads were incubated with the
349 cleared lysate for 1 h at 4°C. All AP samples were washed four times with mRIPA
350 buffer, combined and washed again in mRIPA buffer. The beads were heated in LDS
351 sample buffer, supplemented with 1 mM dithiothreitol (DTT; Sigma, D5545) for 10 min
352 at 70°C and alkylated using 5.5 mM 2-chloroacetamide (CAA; Sigma, C0267) for 30
353 min at RT in the dark (Nielsen et al. 2008).

354 **Sample preparation for the proteome analysis**

355 *MKRN1* KD using siRNA2 was performed in heavy labelled SILAC cells and control
356 KD was performed in light labelled SILAC cells in two replicates. For the third replicate,
357 a label swop was performed, knocking down *MKRN1* (siRNA2) in light labelled SILAC
358 cells and control in heavy labelled SILAC cells. For proteome analysis, cells were lysed
359 as described above. Subsequently, 25 µg protein from each SILAC condition (50 µg in
360 total) were pooled and processed as described below.

361 **Sample preparation for mass spectrometry**

362 The enriched proteins were resolved by SDS-PAGE on a NuPAGE 4-12% Bis-Tris
363 protein gel (Thermo Fisher Scientific) and stained using the Colloidal Blue Staining Kit
364 (Life Technologies). Proteins were in-gel digested using trypsin, before peptides were
365 extracted from the gel. To concentrate, clear and acidify the peptides, they were bound
366 to C18 StageTips as described previously (Rappsilber et al. 2007).

367 **Mass spectrometry data acquisition**

368 Peptide fractions were analysed on a quadrupole Orbitrap mass spectrometer (Thermo
369 Q Exactive Plus, Thermo Scientific) coupled to an uHPLC system (EASY-nLC 1000,
370 Thermo Scientific) (Michalski et al. 2011). Peptide samples were separated on a C18
371 reversed phase column (length: 20 cm, inner diameter: 75 μ m, bead size: 1.9 μ m) and
372 eluted in a linear gradient from 8 to 40% acetonitrile containing 0.1% formic acid in 105
373 min for the interactome analyses, in 175 min for the proteome analyses, or in 125 min
374 for the ubiquitylome analyses. The mass spectrometer was operated in data-
375 dependent positive mode, automatically switching between MS and MS² acquisition.
376 The full scan MS spectra (m/z 300–1650) were acquired in the Orbitrap. Sequential
377 isolation and fragmentation of the ten most abundant ions was performed by higher-
378 energy collisional dissociation (HCD) (Olsen et al. 2007). Peptides with unassigned
379 charge states, as well as with charge states less than +2 were excluded from
380 fragmentation. The Orbitrap mass analyser was used for acquisition of fragment
381 spectra.

382 **Peptide identification and quantification**

383 Raw data files were analysed and peptides were identified using the MaxQuant
384 software (version 1.5.28) (Cox et al. 2009). Parent ion and MS² spectra were compared
385 to a database containing 92,578 human protein sequences obtained from UniProtKB
386 (release June 2018), coupled to the Andromeda search engine (Cox et al. 2011).
387 Cysteine carbamidomethylation was set as a fixed modification. N-terminal acetylation,
388 oxidation, and N-ethylmaleimide (NEM) were set as variable modifications. For
389 ubiquitylome data analysis, glycine-glycine (GlyGly) modification of lysine was
390 additionally set as a variable modification. The mass tolerance for the spectra search
391 was set to be lower than 6 ppm in MS and 20 ppm in HCD MS² mode. Spectra were

392 searched with strict trypsin specificity and allowing for up to three mis-cleavages. Site
393 localisation probabilities were determined by MaxQuant using the PTM scoring
394 algorithm as described previously (Elias and Gygi 2007; Cox and Mann 2008). Filtering
395 of the dataset was based on the posterior error probability to arrive at a false discovery
396 rate (FDR) < 1% estimated using a target-decoy approach. Proteins that were
397 categorised as “only identified by site”, potential contaminants and reverse hits were
398 removed. Only proteins identified with at least two peptides (including at least one
399 unique peptide) and a SILAC ratio count of at least two were used for analysis. For AP
400 experiments, proteins that were quantified in at least two out of three experiments were
401 kept for further analysis. In total, we quantified 1,106 and 1,097 protein groups in the
402 AP experiments with GFP-MKRN1^{wt} (**Fig. 1A**), GFP-MKRN1^{PAM2mut} (**Fig. 1D**) and
403 GFP-MKRN1^{RINGmut} (**Supplemental Fig. S7**), respectively (**Supplemental Table S1**).
404 The SILAC ratios were log₂ transformed and converted into an asymmetric z-score
405 based on the mean and interquartile range of the distribution as described previously
406 (Cox and Mann 2008). For statistical analysis, a moderated t-test from the limma
407 algorithm was used (Ritchie et al. 2015). Enriched proteins with an FDR < 5% were
408 determined to be significantly enriched interactors (for GFP-MKRN1^{wt}). For proteins
409 enriched in GFP-MKRN1^{RINGmut} over GFP-MKRN1^{wt}, proteins with an FDR < 5% and
410 a GFP-MKRN1^{wt}/GFP z-score > 1 were selected. In the proteome experiment, we
411 quantified 6,439 protein groups, present in all three replicates. Ratio-ratio and ratio-
412 intensity plots were created in R (version 3.4.3) using RStudio
413 (<http://www.rstudio.com/>).

414 **Functional annotation of MKRN1 interactors and MKRN1-ubiquitylation targets.**

415 In order to assess the functions of MKRN1-interacting proteins and proteins with
416 MKRN1-dependent ubiquitylation sites, we performed gene ontology (GO) enrichment

417 analyses using the Database for Annotation, Visualization and Integrated Discovery
418 (DAVID 6.7) for three GO domains (Jiao et al. 2012). Enriched GO terms (modified
419 Fisher exact test, adjusted P value < 0.05, Benjamini-Hochberg correction;
420 **Supplemental Fig. S2B, S8A**) were visualised using REVIGO (Reduce & Visualize
421 Gene Ontology) allowing medium GO term similarity (Supek et al. 2011).

422 **Western blot**

423 Denatured proteins were separated by SDS-PAGE on a NuPAGE 4-12% Bis-Tris
424 protein gel (Life Technologies) and transferred to a 0.45 μ m nitrocellulose membrane
425 (VWR). For detection, either fluorophore-coupled secondary antibodies or HRP-
426 conjugated secondary antibodies and WesternBright Chemiluminescent Substrate
427 (Biozym Scientific) or SuperSignal West Pico Chemiluminescent Substrate (Life
428 Technologies) were used. Western blots were quantified by determining the
429 background-subtracted densities of the protein of interest using ImageJ (Schindelin et
430 al. 2015). The signal from the AP (against GFP-tagged protein of interest) was
431 normalised to the respective control samples expressing the empty vector or to the
432 input.

433 **Antibodies**

434 The following antibodies were used: anti-GFP (B-2 clone; Santa Cruz; sc-9996), anti-
435 MKRN1 (Bethyl Laboratories, A300-990A), anti-PABPC1/3 (Cell Signaling, 4992), anti-
436 Znf598 (N1N3; GeneTex; GTX119245), anti- α Tubulin (Sigma Aldrich, T-5168), anti-
437 Rabbit IgG (Cell Signaling; 7074), anti-Mouse IgG (Cell Signaling; 7076), IRDye®
438 680RD Goat anti-Mouse IgG (P/N 925-68070), and IRDye® 800CW Goat anti-Rabbit
439 IgG (P/N 925-32211) (both LI-COR Biosciences GmbH).

440 **RNA isolation, cDNA synthesis and qPCR**

441 Cells were washed twice in ice-cold PBS and harvested. RNA was isolated using the
442 RNeasy Plus Mini Kit (Qiagen) according to the manufacturer's recommendations.
443 500 ng total RNA was transcribed into cDNA using random hexamer primers (Thermo
444 Scientific) and the RevertAid Reverse Transcriptase (Thermo Scientific) according to
445 the manufacturer's recommendations. qPCR was performed using the Luminaris
446 HiGreen qPCR Master Mix, low ROX (Thermo Scientific) according to the
447 manufacturer's recommendations with 10 μ M forward and reverse primers
448 **(Supplemental Table S5).**

449 **iCLIP experiments and data processing**

450 iCLIP libraries were prepared as described previously (Huppertz et al. 2014; Sutandy
451 et al. 2016). HEK293T cells ectopically expressing either GFP alone (empty vector) or
452 N-terminally GFP-tagged MKRN1 wild type (GFP-MKRN1^{wt}), GFP-MKRN1^{PAM2mut}, or
453 GFP-MKRN1^{RINGmut} were used. For crosslinking, confluent cells were irradiated once
454 with 150 mJ/cm² at 254 nm in a Stratalinker 2400 or treated with 4-thiouridine (100 μ M
455 for 16 h) and irradiated with 3x 300 mJ/cm² in a Stratalinker 2400 with 365 nm bulbs.
456 For IP, 10.5 μ g anti-GFP antibody (goat, Protein Unit, MPI-CBG, Dresden) were used
457 per sample. The libraries were sequenced as 50-nt single-end reads on an Illumina
458 MiSeq platform **(Supplemental Table S2).**

459 Basic sequencing quality checks were applied to all reads using FastQC (version
460 0.11.5) (<https://www.bioinformatics.babraham.ac.uk/projects/fastqc/>). Afterwards,
461 reads were filtered based on sequencing qualities (Phred score) of the barcode region.
462 Only reads with at most one position with a sequencing quality < 20 in the experimental
463 barcode (positions 4 to 7) and without any position with a sequencing quality < 17 in
464 the random barcode (positions 1-3 and 8-9) were kept for further analysis. Remaining

465 reads were de-multiplexed based on the experimental barcode on positions 4 to 7
466 using Flexbar (version 3.0.0) (Dodt et al. 2012) without allowing mismatches.

467 All following steps of the analysis were performed on all individual samples after de-
468 multiplexing. Remaining adapter sequences were trimmed from the right end of the
469 reads using Flexbar (version 3.0.0) allowing up to one mismatch in 10 nt, requiring a
470 minimal overlap of 1 nt of read and adapter. After trimming off the adapter, the barcode
471 is trimmed off of the left end of the reads (first 9 nt) and added to the header of the
472 read, such that the information is kept available for downstream analysis. Reads
473 shorter than 15 nt were removed from further analysis.

474 Trimmed and filtered reads were mapped to the human genome (assembly version
475 GRCh38) and its annotation based on GENCODE release 25 (Harrow et al. 2012)
476 using STAR (version 2.5.4b) (Dobin et al. 2013). When running STAR, up to two
477 mismatches were allowed, soft-clipping was prohibited and only uniquely mapping
478 reads were kept for further analysis.

479 Following mapping, duplicate reads were marked using the dedup function of bamUtil
480 (version 1.0.13), which defines duplicates as reads whose 5' ends map to the same
481 position in the genome (<https://github.com/statgen/bamUtil>). Subsequently, marked
482 duplicates with identical random barcodes were removed since they are considered
483 technical duplicates, while biological duplicates showing unequal random barcodes
484 were kept.

485 Resulting bam files were sorted and indexed using SAMtools (version 1.5) (Li et al.
486 2009). Based on the bam files, bedgraph files were created using bamToBed of the
487 BEDTools suite (version 2.25.0) (Quinlan and Hall 2010), considering only the position
488 upstream of the 5' mapping position of the read, since this nucleotide is considered as

489 the crosslinked nucleotide. bedgraph files were then transformed to bigWig file format
490 using bedGraphToBigWig of the UCSC tool suite (Kent et al. 2010).

491 **Identification and characterisation of MKRN1 binding sites**

492 Peak calling was performed on merged iCLIP coverage tracks (crosslink events per
493 nucleotide) from the three replicates based on GENCODE annotation (release 27,
494 GRCh38) using ASPeak (version 2.0; default setting plus `-nornaseq` to estimate
495 parameters p and r for the negative binomial distributions in a 500-nt window around
496 each peak) (Kucukural et al. 2013). The initially predicted peaks were resized to
497 uniform 9-nt windows around their weighted centred as defined by ASPeak. To avoid
498 artefacts, we removed sparsely covered peaks that harbour crosslink events on less
499 than three nucleotides within the 9-nt region window. We iteratively merged all
500 remaining windows if overlapping by at least 1 nt, by defining the position with the
501 cumulative half maximum count of crosslink events as new window centre. We further
502 kept only reproducible windows with at least three crosslink events from any two
503 replicates. Finally, we excluded all windows overlapping with none or multiple protein-
504 coding genes (GENCODE annotations support level ≥ 2 and transcript support level \geq
505 3), and assign each binding site to a distinct genomic region (3' UTR, 5' UTR, CDS,
506 intron). Consistent with the mostly cytoplasmic localisation of MKRN1 (Miroci et al.
507 2012; Cassar et al. 2015; Hildebrandt et al. 2017), less than 6% of the binding sites
508 were predicted within introns, which were excluded from further analysis. This
509 procedure yielded a total of 7,331 MKRN1 binding sites in 2,163 genes.

510 In order to estimate binding site strength and to facilitate comparisons between binding
511 sites (**Fig. 2B,D** and **Supplemental Fig. 3D-F, 4A,C,D**), we corrected for transcript
512 abundance by representing the crosslink events within a binding site as a 'signal-over-
513 background' ratio (SOB). The respective background was calculated as the sum of

514 crosslink events outside of binding sites (plus 5 nt to either side) by the merged length
515 of all exons. 3' UTR lengths were restricted to 10 nt past the last MKRN1 binding site
516 or 500 nt if no binding site was present. SOB calculations were performed separately
517 for each replicate and then averaged. No SOB value was assigned for genes with a
518 background of < 10 crosslink events, resulting in SOB values for 97% of all binding
519 sites.

520 In order to assess the local RNA sequence context of MKRN1 binding sites (**Fig. 2B**
521 and **Supplemental Fig. S4A**), enriched 4-mers were counted inside the 9-nt binding
522 sites as well as within 40-nt before and after. To estimate an empirical background
523 distribution, 1,000 9-nt windows were randomly picked in 3' UTRs and 4-mer
524 frequencies were counted in the same windows. This process was repeated 100 times,
525 and the resulting mean and standard deviation were used to calculate the z-score for
526 each 4-mer.

527 In order to define the A-rich regions downstream of MKRN1 binding sites in 3' UTRs
528 (A-rich stretches), we used a maximisation approach in a 55-nt search space starting
529 from the binding site centre. Within this space, we calculated the percentage of A
530 nucleotides (A-content) for windows of increasing size (8-30 nt) and selected the
531 stretch with highest value for each window size. In case of ties, the window closer to
532 the binding site was preferred, resulting in a set of 23 candidate A-stretches with the
533 maximal A-content for each length. Next, we computed the longest continuous A run
534 (LCA) and a weighted A-content (multiplying the A-content with the number of A
535 nucleotides) for each candidate A-stretch. Candidate A-stretches with an A-content <
536 70%, a weighted A-content < 11 and an LCA < 4 were excluded. The final A-stretch
537 for each binding site was then selected in a hierarchical manner, preferring LCA over
538 weighted A-content. Lastly, overlapping A-stretches of neighbouring binding sites were

539 merged by selecting the highest scoring A-stretch, based on LCA and weighted A-
540 content. In total, this procedure identified 1,412 non-overlapping A-stretches,
541 associated with 1,848 binding sites.

542 In order to estimate the extent of MKRN1 binding to poly(A) tails (**Fig. 3B**), we
543 evaluated the percentage of adenosine within the iCLIP reads that could not be
544 mapped to the human genome without soft-clipping (see above). iCLIP data for
545 heterogeneous nuclear ribonucleoprotein H (HNRNPH) served as control (Braun et
546 al. 2018). Annotated transcript 3' ends were taken from GENCODE (all annotated
547 protein-coding transcripts with support level ≤ 2 and transcript support level ≤ 3 ;
548 release 28, GRCh38.p12; www.gencodegenes.org). For **Fig. 3C**, all crosslink events
549 within a 2-kb window around the annotated transcripts 3' ends for 3' UTR longer than
550 1 kb were counted.

551 **Evolutionary characterisation of Makorin protein family**

552 Four different ortholog searches were performed using HaMStR-OneSeq (Ebersberger
553 et al. 2014) against the Quest for Orthologs Consortium protein set, containing 78
554 species (release 2017_04) (Sonnhammer et al. 2014). For each run, a different seed
555 protein was chosen: human MKRN1-3 (UniProt identifiers Q9UHC7, Q9H000 and
556 Q13064) and MKRN4 from zebrafish (A9C4A6). In order to identify proteins with a
557 similar domain architecture, we calculated a unidirectional feature architecture
558 similarity (FAS) score which compares the domain architecture of the seed protein and
559 the predicted ortholog (Koestler et al. 2010). Predicted orthologues with FAS < 0.7
560 were removed after initial assessment. Finally, all vertebrate species and selected
561 invertebrate species were used for reconstruction of a maximum likelihood (ML) tree.
562 For this, protein sequences were aligned using MAFFT v7.294b L-INS-i (Kato and
563 Standley 2013), and ML trees with 100 bootstrap replicates were calculated using

564 RAXML version 8.1.9 (Stamatakis 2014). Settings for a rapid bootstrap analysis and
565 searching for the best scoring ML tree in one program run (-f a) and an automatic
566 selection of the best fitting amino acid substitution model (-m PROTGAMMAAUTO)
567 were chosen. Reconstructed trees were visualised using FigTree v1.4.2
568 (<http://tree.bio.ed.ac.uk/software/figtree/>).

569 The phylogenetic tree and FASTA sequences from the ortholog dataset were loaded
570 into DoMosaics (<http://www.domosaics.net>) and Pfam domains were annotated with
571 HMMER (<http://hmmer.org/>, default parameters). Since the PAM2 motif in all Makorin
572 proteins differs from the described consensus motif (Albrecht and Lengauer 2004), a
573 custom Hidden Markov Model was trained on PAM2 motifs from selected Makorin
574 orthologs and used for a HMMER scan of the orthologs (no E-value cutoff). The same
575 procedure was repeated for the PAM2-like motif (PAM2L) (Pohlmann et al. 2015).

576 **Dual fluorescence translation stall assay via flow cytometry**

577 Knockdowns were performed for 24 h, before the dual fluorescence reporter plasmids
578 were ectopically expressed for 48 h. Cells were washed in PBS and trypsinised. After
579 sedimentation, cells were resuspended in DPBS supplemented with 2 mM EDTA.
580 Cellular GFP and RFP fluorescence was measured using flow cytometry on a
581 LSRFortessa SORP (BD Biosciences). Data analysis was done using FlowJo (v10)
582 (FlowJo, LLC). For statistical testing, paired two-tailed Student's t-tests with Benjamini-
583 Hochberg correction were performed on $n \geq 6$ replicates.

584 **Ubiquitin remnant profiling**

585 Di-glycine remnant profiling was performed as described before (Wagner et al. 2011;
586 Heidelberger et al. 2018). In four different experiments, isotope labels were assigned
587 as follows: experiment 1, *MKRN1* KD1 (siRNA1), *MKRN1* KD2 (siRNA2) and control
588 siRNA with light, medium and heavy SILAC labels, respectively; experiment 2, *MKRN1*

589 KD2 (siRNA2) and control siRNA with heavy and light SILAC labels, respectively;
590 experiment 3, *MKRN1* KD2 (siRNA2) and control siRNA with heavy and light SILAC
591 labels, respectively; experiment 3, *MKRN1* KD2 (siRNA2) and control siRNA with light
592 and heavy SILAC labels, respectively. Cells were treated with the proteasome
593 inhibitors bortezomib (1 μ M, 8h, replicate 1; Santa Cruz Biotechnology) or MG132 (10
594 μ M, 2 h, replicates 2, 3, 4; Sigma). Proteins were precipitated in acetone. Proteins
595 were digested with endoproteinase Lys-C (Wako Chemicals) and sequencing-grade
596 modified trypsin (Sigma). To purify the peptides, reversed-phase Sep-Pak C18
597 cartridges (Waters) were used. Modified peptides were enriched using di-glycine-
598 lysine antibody resin (Cell Signaling Technology). The enriched peptides were eluted
599 with 0.15% trifluoroacetic acid in water, then fractionated using micro-column-based
600 strong-cation exchange chromatography (SCX) (Weinert et al. 2013) before being
601 desalted on reversed-phase C18 StageTips (Rappsilber et al. 2007). Samples were
602 analysed by quantitative mass spectrometry and MaxQuant as described above. To
603 identify significantly regulated ubiquitylation sites, the limma algorithm was applied
604 (Ritchie et al. 2015). A p-value < 0.1 after multiple testing correction was used as a
605 cut-off to determine up- and downregulated ubiquitylation sites. Volcano and dot plots
606 were created in R (version 3.4.3).

607 **Functional interaction network of MKRN1 ubiquitylation target proteins**

608 The functional protein interaction network analysis was performed by integrating
609 interaction data from the STRING database (score > 0.4), the BioGrid database and
610 our own findings (Franceschini et al. 2013; Chatr-Aryamontri et al. 2017). Cytoscape
611 (version 3.6.1) was used to visualise the protein interaction network (Saito et al. 2012).

612 **Data availability**

613 The mass spectrometry proteomics data have been deposited to the
614 ProteomeXchange Consortium (<http://proteomecentral.proteomexchange.org>) via the
615 PRIDE partner repository with the dataset identifier PXD011772. Raw and processed
616 iCLIP data are available at GEO under the accession number GSE122869.

617 **Acknowledgements**

618 We would like to thank all members of the Zarnack, König and Beli labs, as well as
619 René Ketting, Nadine Wittkopp and Miguel Almeida for fruitful discussions. The authors
620 gratefully thank the Ramanujan S. Hegde for providing the dual fluorescence reporter
621 plasmids. We thank Anja Freiwald for assistance with mass spectrometry analysis and
622 Dr. Stefan Simm for assistance with evaluating PAM2 mutations. The support of the
623 IMB Core Facilities Bioinformatics, Flow Cytometry, Genomics, and the use of its
624 Illumina MiSeq, as well as the DFG-funded Mass Spectrometer Q Exactive Plus (INST
625 247/766-1 FUGG) are gratefully acknowledged. K.Z. was supported by the LOEWE
626 program Ubiquitin Networks (Ub-Net) of the State of Hesse (Germany) and the SFB
627 902 of the German Research Foundation. P.B. is supported by the Emmy Noether
628 Program (BE 5342/1-1), the SFB 1177 of the German Research Foundation and the
629 Marie Curie Career Integration Grant from the European Commission (grant
630 agreement number: 630763). The project was funded by the German Research
631 Foundation (DFG) as part of SPP1925 to J.-Y.R. (RO 4681/4-1) and J.K. (KO 4566/3-
632 1). Animal shapes in Supplemental Fig. S1A were obtained from PhyloPic and are
633 used under the Creative Common Attribution-NonCommercial-ShareAlike 3.0
634 Unported license.

635 **Author contributions**

636 A.H. performed iCLIP experiments, flow cytometry measurements of dual fluorescence
637 reporters and most proteomics experiments. M.B. performed most bioinformatics

638 analyses of MKRN1 iCLIP data. C.R. analysed MKRN1 binding at transcript 3' ends
639 and poly(A) tails. A.B. and S.B. performed initial iCLIP data processing and analysis.
640 A.H. and A.B. analysed the proteomics data. J.B.H. and A.V. contributed to replicate
641 ubiquitin remnant profiling experiments and AP-Western blot experiments,
642 respectively. H.H. performed replicate iCLIP and replicate AP-Western blot
643 experiments. C.R. and I.E. contributed evolutionary characterisation of Makorin
644 proteins. A.D. and J.-Y.R. performed complementary studies in *D. melanogaster*. S.E.
645 and K.Z. supervised the bioinformatics analyses. J.K. and P.B. conceived the project
646 with K.Z. and supervised the experimental work. A.H., J.K., K.Z. and P.B. wrote the
647 manuscript with help and comments from all co-authors.

648 **References**

- 649 Albrecht M, Lengauer T. 2004. Survey on the PABC recognition motif PAM2. *Biochem*
650 *Biophys Res Commun* **316**: 129-138.
- 651 Arthur L, Pavlovic-Djuranovic S, Smith-Koutmou K, Green R, Szczesny P, Djuranovic
652 S. 2015. Translational control by lysine-encoding A-rich sequences. *Sci Adv* **1**.
- 653 Bag J. 2001. Feedback inhibition of poly(A)-binding protein mRNA translation. A
654 possible mechanism of translation arrest by stalled 40 S ribosomal subunits. *J*
655 *Biol Chem* **276**: 47352-47360.
- 656 Bengtson MH, Joazeiro CA. 2010. Role of a ribosome-associated E3 ubiquitin ligase
657 in protein quality control. *Nature* **467**: 470-473.
- 658 Böhne A, Darras A, D'Cotta H, Baroiller JF, Galiana-Arnoux D, Volf JN. 2010. The
659 vertebrate makorin ubiquitin ligase gene family has been shaped by large-scale
660 duplication and retroposition from an ancestral gonad-specific, maternal-effect
661 gene. *BMC Genomics* **11**: 721.
- 662 Brandman O, Hegde RS. 2016. Ribosome-associated protein quality control. *Nat*
663 *Struct Mol Biol* **23**: 7-15.
- 664 Brandman O, Stewart-Ornstein J, Wong D, Larson A, Williams CC, Li GW, Zhou S,
665 King D, Shen PS, Weibezahn J et al. 2012. A ribosome-bound quality control
666 complex triggers degradation of nascent peptides and signals translation stress.
667 *Cell* **151**: 1042-1054.
- 668 Braun S, Enculescu M, Setty ST, Cortés-López M, de Almeida BP, Sutandy FXR,
669 Schulz L, Busch A, Seiler M, Ebersberger S et al. 2018. Decoding a cancer-
670 relevant splicing decision in the *RON* proto-oncogene using high-throughput
671 mutagenesis. *Nat Commun* **9**: 3315.
- 672 Cassar PA, Carpenedo RL, Samavarchi-Tehrani P, Olsen JB, Park CJ, Chang WY,
673 Chen Z, Choey C, Delaney S, Guo H et al. 2015. Integrative genomics positions
674 MKRN1 as a novel ribonucleoprotein within the embryonic stem cell gene
675 regulatory network. *EMBO Rep* **16**: 1334-1357.
- 676 Chatr-Aryamontri A, Oughtred R, Boucher L, Rust J, Chang C, Kolas NK, O'Donnell L,
677 Oster S, Theesfeld C, Sellam A et al. 2017. The BioGRID interaction database:
678 2017 update. *Nucleic Acids Res* **45**: D369-D379.
- 679 Choe YJ, Park SH, Hassemer T, Korner R, Vincenz-Donnelly L, Hayer-Hartl M, Hartl
680 FU. 2016. Failure of RQC machinery causes protein aggregation and
681 proteotoxic stress. *Nature* **531**: 191-195.

- 682 Chu J, Hong NA, Masuda CA, Jenkins BV, Nelms KA, Goodnow CC, Glynne RJ, Wu
683 H, Masliah E, Joazeiro CA et al. 2009. A mouse forward genetics screen
684 identifies LISTERIN as an E3 ubiquitin ligase involved in neurodegeneration.
685 *Proc Natl Acad Sci U S A* **106**: 2097-2103.
- 686 Collaboration O. 2016. The ORFeome Collaboration: a genome-scale human ORF-
687 clone resource. *Nat Methods* **13**: 191-192.
- 688 Cox J, Mann M. 2008. MaxQuant enables high peptide identification rates,
689 individualized p.p.b.-range mass accuracies and proteome-wide protein
690 quantification. *Nat Biotechnol* **26**: 1367-1372.
- 691 Cox J, Matic I, Hilger M, Nagaraj N, Selbach M, Olsen JV, Mann M. 2009. A practical
692 guide to the MaxQuant computational platform for SILAC-based quantitative
693 proteomics. *Nat Protoc* **4**: 698-705.
- 694 Cox J, Neuhauser N, Michalski A, Scheltema RA, Olsen JV, Mann M. 2011.
695 Andromeda: a peptide search engine integrated into the MaxQuant environment.
696 *J Proteome Res* **10**: 1794-1805.
- 697 Deo RC, Sonenberg N, Burley SK. 2001. X-ray structure of the human hyperplastic
698 discs protein: an ortholog of the C-terminal domain of poly(A)-binding protein.
699 *Proc Natl Acad Sci U S A* **98**: 4414-4419.
- 700 Dobin A, Davis CA, Schlesinger F, Drenkow J, Zaleski C, Jha S, Batut P, Chaisson M,
701 Gingeras TR. 2013. STAR: ultrafast universal RNA-seq aligner. *Bioinformatics*
702 **29**: 15-21.
- 703 Dodt M, Roehr JT, Ahmed R, Dieterich C. 2012. FLEXBAR-Flexible Barcode and
704 Adapter Processing for Next-Generation Sequencing Platforms. *Biology (Basel)*
705 **1**: 895-905.
- 706 Ebersberger I, Simm S, Leisegang MS, Schmitzberger P, Mirus O, von Haeseler A,
707 Bohnsack MT, Schleiff E. 2014. The evolution of the ribosome biogenesis
708 pathway from a yeast perspective. *Nucleic Acids Res* **42**: 1509-1523.
- 709 Elias JE, Gygi SP. 2007. Target-decoy search strategy for increased confidence in
710 large-scale protein identifications by mass spectrometry. *Nat Methods* **4**: 207-
711 214.
- 712 Franceschini A, Szklarczyk D, Frankild S, Kuhn M, Simonovic M, Roth A, Lin J,
713 Minguéz P, Bork P, von Mering C et al. 2013. STRING v9.1: protein-protein
714 interaction networks, with increased coverage and integration. *Nucleic Acids*
715 *Res* **41**: D808-815.
- 716 Garzia A, Jafarnejad SM, Meyer C, Chapat C, Gogakos T, Morozov P, Amiri M, Shapiro
717 M, Molina H, Tuschl T et al. 2017. The E3 ubiquitin ligase and RNA-binding

- 718 protein ZNF598 orchestrates ribosome quality control of premature
719 polyadenylated mRNAs. *Nat Commun* **8**: 16056.
- 720 Gray TA, Hernandez L, Carey AH, Schaldach MA, Smithwick MJ, Rus K, Marshall
721 Graves JA, Stewart CL, Nicholls RD. 2000. The ancient source of a distinct gene
722 family encoding proteins featuring RING and C(3)H zinc-finger motifs with
723 abundant expression in developing brain and nervous system. *Genomics* **66**:
724 76-86.
- 725 Hafner M, Landthaler M, Burger L, Khorshid M, Hausser J, Berninger P, Rothballer A,
726 Ascano M, Jr., Jungkamp AC, Munschauer M et al. 2010. Transcriptome-wide
727 identification of RNA-binding protein and microRNA target sites by PAR-CLIP.
728 *Cell* **141**: 129-141.
- 729 Harrow J, Frankish A, Gonzalez JM, Tapanari E, Diekhans M, Kokocinski F, Aken BL,
730 Barrell D, Zadissa A, Searle S et al. 2012. GENCODE: the reference human
731 genome annotation for The ENCODE Project. *Genome Res* **22**: 1760-1774.
- 732 Heidelberg JB, Voigt A, Borisova ME, Petrosino G, Ruf S, Wagner SA, Beli P. 2018.
733 Proteomic profiling of VCP substrates links VCP to K6-linked ubiquitylation and
734 c-Myc function. *EMBO Rep* **19**.
- 735 Higgins R, Gendron JM, Rising L, Mak R, Webb K, Kaiser SE, Zuzow N, Riviere P,
736 Yang B, Fenech E et al. 2015. The Unfolded Protein Response Triggers Site-
737 Specific Regulatory Ubiquitylation of 40S Ribosomal Proteins. *Mol Cell* **59**: 35-
738 49.
- 739 Hildebrandt A, Alanis-Lobato G, Voigt A, Zarnack K, Andrade-Navarro MA, Beli P,
740 König J. 2017. Interaction profiling of RNA-binding ubiquitin ligases reveals a
741 link between posttranscriptional regulation and the ubiquitin system. *Sci Rep* **7**:
742 16582.
- 743 Huppertz I, Attig J, D'Ambrogio A, Easton LE, Sibley CR, Sugimoto Y, Tajnik M, König
744 J, Ule J. 2014. iCLIP: protein-RNA interactions at nucleotide resolution.
745 *Methods* **65**: 274-287.
- 746 Jamar NH, Kritsiligkou P, Grant CM. 2018. Loss of mRNA surveillance pathways
747 results in widespread protein aggregation. *Sci Rep* **8**: 3894.
- 748 Jiao X, Sherman BT, Huang da W, Stephens R, Baseler MW, Lane HC, Lempicki RA.
749 2012. DAVID-WS: a stateful web service to facilitate gene/protein list analysis.
750 *Bioinformatics* **28**: 1805-1806.
- 751 Joazeiro CAP. 2017. Ribosomal Stalling During Translation: Providing Substrates for
752 Ribosome-Associated Protein Quality Control. *Annu Rev Cell Dev Biol* **33**: 343-
753 368.

- 754 Juszkiwicz S, Chandrasekaran V, Lin Z, Kraatz S, Ramakrishnan V, Hegde RS. 2018.
755 ZNF598 Is a Quality Control Sensor of Collided Ribosomes. *Mol Cell* **72**: 469-
756 481 e467.
- 757 Juszkiwicz S, Hegde RS. 2017. Initiation of Quality Control during Poly(A) Translation
758 Requires Site-Specific Ribosome Ubiquitination. *Mol Cell* **65**: 743-750 e744.
- 759 Kaida D, Berg MG, Younis I, Kasim M, Singh LN, Wan L, Dreyfuss G. 2010. U1 snRNP
760 protects pre-mRNAs from premature cleavage and polyadenylation. *Nature*
761 **468**: 664-668.
- 762 Katoh K, Standley DM. 2013. MAFFT multiple sequence alignment software version 7:
763 improvements in performance and usability. *Mol Biol Evol* **30**: 772-780.
- 764 Kent WJ, Zweig AS, Barber G, Hinrichs AS, Karolchik D. 2010. BigWig and BigBed:
765 enabling browsing of large distributed datasets. *Bioinformatics* **26**: 2204-2207.
- 766 Kim JH, Park KW, Lee EW, Jang WS, Seo J, Shin S, Hwang KA, Song J. 2014.
767 Suppression of PPAR γ through MKRN1-mediated ubiquitination and
768 degradation prevents adipocyte differentiation. *Cell Death Differ* **21**: 594-603.
- 769 Kim JH, Park SM, Kang MR, Oh SY, Lee TH, Muller MT, Chung IK. 2005. Ubiquitin
770 ligase MKRN1 modulates telomere length homeostasis through a proteolysis of
771 hTERT. *Genes Dev* **19**: 776-781.
- 772 Ko A, Shin JY, Seo J, Lee KD, Lee EW, Lee MS, Lee HW, Choi IJ, Jeong JS, Chun
773 KH et al. 2012. Acceleration of gastric tumorigenesis through MKRN1-mediated
774 posttranslational regulation of p14ARF. *J Natl Cancer Inst* **104**: 1660-1672.
- 775 Koestler T, von Haeseler A, Ebersberger I. 2010. FACT: functional annotation transfer
776 between proteins with similar feature architectures. *BMC Bioinformatics* **11**: 417.
- 777 König J, Zarnack K, Rot G, Curk T, Kayikci M, Zupan B, Turner DJ, Luscombe NM,
778 Ule J. 2010. iCLIP reveals the function of hnRNP particles in splicing at
779 individual nucleotide resolution. *Nat Struct Mol Biol* **17**: 909-915.
- 780 Kozlov G, De Crescenzo G, Lim NS, Siddiqui N, Fantus D, Kahvejian A, Trempe JF,
781 Elias D, Ekiel I, Sonenberg N et al. 2004. Structural basis of ligand recognition
782 by PABC, a highly specific peptide-binding domain found in poly(A)-binding
783 protein and a HECT ubiquitin ligase. *EMBO J* **23**: 272-281.
- 784 Kozlov G, Menade M, Rosenauer A, Nguyen L, Gehring K. 2010. Molecular
785 determinants of PAM2 recognition by the MLLE domain of poly(A)-binding
786 protein. *J Mol Biol* **397**: 397-407.
- 787 Kozlov G, Trempe JF, Khaleghpour K, Kahvejian A, Ekiel I, Gehring K. 2001. Structure
788 and function of the C-terminal PABC domain of human poly(A)-binding protein.
789 *Proc Natl Acad Sci U S A* **98**: 4409-4413.

- 790 Kucukural A, Ozadam H, Singh G, Moore MJ, Cenik C. 2013. ASPeak: an abundance
791 sensitive peak detection algorithm for RIP-Seq. *Bioinformatics* **29**: 2485-2486.
- 792 Lee EW, Lee MS, Camus S, Ghim J, Yang MR, Oh W, Ha NC, Lane DP, Song J. 2009.
793 Differential regulation of p53 and p21 by MKRN1 E3 ligase controls cell cycle
794 arrest and apoptosis. *EMBO J* **28**: 2100-2113.
- 795 Letzring DP, Wolf AS, Brule CE, Grayhack EJ. 2013. Translation of CGA codon
796 repeats in yeast involves quality control components and ribosomal protein L1.
797 *RNA* **19**: 1208-1217.
- 798 Li H, Handsaker B, Wysoker A, Fennell T, Ruan J, Homer N, Marth G, Abecasis G,
799 Durbin R, Genome Project Data Processing S. 2009. The Sequence
800 Alignment/Map format and SAMtools. *Bioinformatics* **25**: 2078-2079.
- 801 Lima SA, Chipman LB, Nicholson AL, Chen YH, Yee BA, Yeo GW, Collier J, Pasquinelli
802 AE. 2017. Short poly(A) tails are a conserved feature of highly expressed genes.
803 *Nat Struct Mol Biol* **24**: 1057-1063.
- 804 Lu J, Deutsch C. 2008. Electrostatics in the ribosomal tunnel modulate chain
805 elongation rates. *J Mol Biol* **384**: 73-86.
- 806 Lyabin DN, Eliseeva IA, Skabkina OV, Ovchinnikov LP. 2011. Interplay between Y-
807 box-binding protein 1 (YB-1) and poly(A) binding protein (PABP) in specific
808 regulation of YB-1 mRNA translation. *RNA Biol* **8**: 883-892.
- 809 Michalski A, Damoc E, Hauschild JP, Lange O, Wieghaus A, Makarov A, Nagaraj N,
810 Cox J, Mann M, Horning S. 2011. Mass spectrometry-based proteomics using
811 Q Exactive, a high-performance benchtop quadrupole Orbitrap mass
812 spectrometer. *Mol Cell Proteomics* **10**: M111 011015.
- 813 Miroci H, Schob C, Kindler S, Olschlager-Schutt J, Fehr S, Jungenitz T, Schwarzacher
814 SW, Bagni C, Mohr E. 2012. Makorin ring zinc finger protein 1 (MKRN1), a novel
815 poly(A)-binding protein-interacting protein, stimulates translation in nerve cells.
816 *J Biol Chem* **287**: 1322-1334.
- 817 Nielsen ML, Vermeulen M, Bonaldi T, Cox J, Moroder L, Mann M. 2008.
818 Iodoacetamide-induced artifact mimics ubiquitination in mass spectrometry. *Nat*
819 *Methods* **5**: 459-460.
- 820 Olsen JV, Macek B, Lange O, Makarov A, Horning S, Mann M. 2007. Higher-energy
821 C-trap dissociation for peptide modification analysis. *Nat Methods* **4**: 709-712.
- 822 Omwanicha J, Zhou XF, Chen SY, Baslan T, Fisher CJ, Zheng Z, Cai C, Shemshedini
823 L. 2006. Makorin RING finger protein 1 (MKRN1) has negative and positive
824 effects on RNA polymerase II-dependent transcription. *Endocrine* **29**: 363-373.

- 825 Pohlmann T, Baumann S, Haag C, Albrecht M, Feldbrügge M. 2015. A FYVE zinc
826 finger domain protein specifically links mRNA transport to endosome trafficking.
827 *Elife* **4**.
- 828 Quinlan AR, Hall IM. 2010. BEDTools: a flexible suite of utilities for comparing genomic
829 features. *Bioinformatics* **26**: 841-842.
- 830 Rappsilber J, Mann M, Ishihama Y. 2007. Protocol for micro-purification, enrichment,
831 pre-fractionation and storage of peptides for proteomics using StageTips. *Nat*
832 *Protoc* **2**: 1896-1906.
- 833 Ritchie ME, Phipson B, Wu D, Hu Y, Law CW, Shi W, Smyth GK. 2015. limma powers
834 differential expression analyses for RNA-sequencing and microarray studies.
835 *Nucleic Acids Res* **43**: e47.
- 836 Saito R, Smoot ME, Ono K, Ruscheinski J, Wang PL, Lotia S, Pico AR, Bader GD,
837 Ideker T. 2012. A travel guide to Cytoscape plugins. *Nat Methods* **9**: 1069-1076.
- 838 Salvatico J, Kim JH, Chung IK, Muller MT. 2010. Differentiation linked regulation of
839 telomerase activity by Makorin-1. *Mol Cell Biochem* **342**: 241-250.
- 840 Schindelin J, Rueden CT, Hiner MC, Eliceiri KW. 2015. The ImageJ ecosystem: An
841 open platform for biomedical image analysis. *Mol Reprod Dev* **82**: 518-529.
- 842 Simms CL, Yan LL, Zaher HS. 2017. Ribosome Collision Is Critical for Quality Control
843 during No-Go Decay. *Mol Cell* **68**: 361-373 e365.
- 844 Simsek D, Tiu GC, Flynn RA, Byeon GW, Leppek K, Xu AF, Chang HY, Barna M. 2017.
845 The Mammalian Ribo-interactome Reveals Ribosome Functional Diversity and
846 Heterogeneity. *Cell* **169**: 1051-1065 e1018.
- 847 Sonnhammer EL, Gabaldon T, Sousa da Silva AW, Martin M, Robinson-Rechavi M,
848 Boeckmann B, Thomas PD, Dessimoz C, Quest for Orthologs c. 2014. Big data
849 and other challenges in the quest for orthologs. *Bioinformatics* **30**: 2993-2998.
- 850 Stamatakis A. 2014. RAxML version 8: a tool for phylogenetic analysis and post-
851 analysis of large phylogenies. *Bioinformatics* **30**: 1312-1313.
- 852 Sundaramoorthy E, Leonard M, Mak R, Liao J, Fulzele A, Bennett EJ. 2017. ZNF598
853 and RACK1 Regulate Mammalian Ribosome-Associated Quality Control
854 Function by Mediating Regulatory 40S Ribosomal Ubiquitylation. *Mol Cell* **65**:
855 751-760 e754.
- 856 Supek F, Bosnjak M, Skunca N, Smuc T. 2011. REVIGO summarizes and visualizes
857 long lists of gene ontology terms. *PLoS One* **6**: e21800.

- 858 Sutandy FXR, Ebersberger S, Huang L, Busch A, Bach M, Kang HS, Fallmann J,
859 Maticzka D, Backofen R, Stadler PF et al. 2018. In vitro iCLIP-based modeling
860 uncovers how the splicing factor U2AF2 relies on regulation by cofactors.
861 *Genome Res* **28**: 699-713.
- 862 Sutandy FXR, Hildebrandt A, König J. 2016. Profiling the Binding Sites of RNA-Binding
863 Proteins with Nucleotide Resolution Using iCLIP. *Methods Mol Biol* **1358**: 175-
864 195.
- 865 Verma R, Oania RS, Kolawa NJ, Deshaies RJ. 2013. Cdc48/p97 promotes
866 degradation of aberrant nascent polypeptides bound to the ribosome. *Elife* **2**:
867 e00308.
- 868 Wagner SA, Beli P, Weinert BT, Nielsen ML, Cox J, Mann M, Choudhary C. 2011. A
869 proteome-wide, quantitative survey of in vivo ubiquitylation sites reveals
870 widespread regulatory roles. *Mol Cell Proteomics* **10**: M111 013284.
- 871 Webster MW, Chen YH, Stowell JAW, Alhusaini N, Sweet T, Graveley BR, Collier J,
872 Passmore LA. 2018. mRNA Deadenylation Is Coupled to Translation Rates by
873 the Differential Activities of Ccr4-Not Nucleases. *Mol Cell* **70**: 1089-1100 e1088.
- 874 Weinert BT, Scholz C, Wagner SA, Iesmantavicius V, Su D, Daniel JA, Choudhary C.
875 2013. Lysine succinylation is a frequently occurring modification in prokaryotes
876 and eukaryotes and extensively overlaps with acetylation. *Cell Rep* **4**: 842-851.
- 877

Supplemental Tables and Legends

Supplemental Tables S1,3,4

Provided as Excel files

Supplemental Tables S2: Summary of MKRN1 iCLIP experiments. iCLIP experiments with GFP-MKRN1 were performed in three independent replicates.

	Sequenced reads	Uniquely mapped reads	Crosslink events	Binding sites
Replicate 1	3,418,021	1,561,445	957,097	-
Replicate 2	6,527,256	3,149,583	1,972,821	-
Replicate 3	4,660,274	2,515,161	2,293,633	-
Total	14,605,551	7,226,189	5,223,551	7,331

Supplemental Table S5: Primers used in this study.

Name	Sequence 5' – 3'	Comment
PAMmut	GCCGTTGCCGGGCAACCCTACTGTGGC	MKRN1 ^{PAM2mut}
	CTCAATAGAATTCACCCAGTCCTCTGAACC	mutant
H307E	CAACTGCAACGAAACCTACTGTCTCAAG	MKRN1 ^{RINGmut}
	GAGAGGATCCCGAAGCGG	mutant
MKRN1 qPCR	CGATACGGGGAGAACTGTGT	<i>MKRN1</i>
	CCTTCTCATGGGCCTCAAT	qPCR primer
ZNF598 qPCR	AACCTCGACAAATGGTCCTG	<i>ZNF598</i>
	GTCTTCGTCCTTGAGCTTCG	qPCR primer
βActin qPCR	TCCTCCCTGGAGAAGAGCTAC	<i>β-actin</i> qPCR
	TGGAGTTGAAGGTAGTTCGTG	primer

Supplemental Table S6: siRNAs used in this study.

Name	Sequence 5' – 3'	Comment
MKRN1 siRNA1	CAGGCGAAGCUGAGUCAAGAA[dT][dT]	Ko et al. 2012

MKRN1 siRNA2	CGGGAUCCUCUCCAACUGCAA[dT][dT]	Kim et al. 2014
ZNF598 siRNA	CCCUCUAAAGUUGGGAAGA[dT][dT]	Sigma, Rosetta predictions
Control siRNA	UGGUUUACAUGUCGACUAA[dT][dT]	Heidelberger et al. 2018

878

Figure legends

Figure 1. MKRN1 interacts with PABP and other regulators of translation and RNA stability. (A) Protein interactome of GFP-MKRN1^{wt} in HEK293T cells analysed by quantitative MS-based proteomics. Combined SILAC ratios (n = 3 replicates) after z-score normalisation are plotted against log₁₀-transformed intensities. 1,100 protein groups were quantified in at least two out of three replicate experiments. MKRN1 and significant interactors are highlighted (FDR < 5%). (B) A PAM2 motif similar to the previously reported consensus (shown on top; **Supplemental Fig. S1B**) (Albrecht and Lengauer 2004) is present in MKRN1 (first amino acid position indicated on the left). Introduced mutations in MKRN1^{PAM2mut} are indicated in red below. Relevant positions are highlighted (**Supplemental Fig. S1B**). (C) Endogenous PABP interacts with MKRN1^{wt} and MKRN1^{RINGmut}, but not with MKRN1^{PAM2mut}. Western blots for endogenous PABPC1 and GFP (two exposure times, exp.) after AP of GFP-MKRN1 (wt and mutants). Ratios of PABP signal (normalised to input) in GFP-MKRN APs over control (GFP empty vector, EV) are shown on the right. Replicates 2, 3, and uncropped gel images are shown in **Supplemental Fig. S9A-C**. (D) Quantitative comparison of the interactomes of GFP-MKRN1^{wt} and GFP-MKRN1^{PAM2mut} shows that PABP and several other interactors are lost upon PAM2 mutation. Combined ratios of three replicates are shown in a scatter plot. Only proteins detected in at least two out of three replicates are shown. MKRN1^{wt} significant interactors (from A) are highlighted as in (A) (FDR < 5% in MKRN1^{wt}).

Figure 2. MKRN1 binds upstream of A-stretches in 3' UTRs. (A) MKRN1 predominantly binds in the 3' UTR of protein-coding genes. Piecharts summarising the distribution of MKRN1 binding sites to different RNA biotypes (7,331 binding sites, left) and different regions within protein-coding transcripts (6,913 binding sites, right). (B) MKRN1 binding sites display a downstream enrichment of AAAA homopolymers. Frequency per nucleotide (nt) for four homopolymeric 4-mers in a 101-nt window around the midpoints of the top 20% MKRN1 binding sites (according to signal-over-background; see Material and methods). (C) MKRN1 crosslink events accumulate upstream of A-stretches. Metaprofile (top) shows the mean crosslink events per nt in a 201-nt window around the start position of 1,412 MKRN1-associated A-stretches in 3' UTRs. Heatmap visualisation (bottom) displays crosslink events per nt (see colour scale) in a 101-nt window around the MKRN1-associated A-stretches. (D) MKRN1 binding site strength (signal-over-background, SOB) increases with length of longest continuous run of A's (LCA) within the A-stretch. Mean and standard deviation of MKRN1 binding sites associated with A-stretches harbouring LCAs of increasing length (x-axis). MKRN1 binding sites without associated A-stretches are shown for comparison on the left. Number of binding sites in each category indicated as barchart above. (E) MKRN1 binds upstream of A-stretches in the 3' UTR of the *LARP1* gene. Genome browser view of GFP-MKRN1 iCLIP data showing crosslink events per nt (merged replicates, turquoise) together with binding sites (lilac) and associated A-stretches (dark green).

Figure 3. MKRN1 binds at poly(A) tails. (A) MKRN1 binds at the annotated transcript 3' end in the *SRSF4* gene. Genome browser view as in **Fig. 2E**. (B) Unmapped MKRN1 iCLIP reads display increased A-content (more than half of all nucleotides in the read), evidencing poly(A) tail binding. Cumulative fraction of iCLIP reads (y-axis, merged replicates) that could not be mapped to the human genome (see Materials and methods) and show at least a given A-content (x-axis). iCLIP data for the unrelated RBP HNRNPH (Braun et al. 2018) are shown for comparison. (C) MKRN1 crosslink events increase towards 3'UTR ends. Metaprofile shows the sum of crosslink events per nt in a 2001-nt window around annotated transcript 3' ends of transcripts with >1 kb 3' UTRs (n = 63,030). (D) Overall RNA binding of MKRN1 is strongly reduced when abrogating PABP interaction. Autoradiograph (left) of UV crosslinking experiments (replicate 1, with 4SU and UV crosslinking at 365 nm; replicates 2 and 3 in **Supplemental Fig. S5**) comparing GFP-MKRN1^{PAM2mut} with GFP-MKRN1^{wt} at different dilution steps for calibration. Quantification of radioactive signal of protein-RNA complexes and corresponding Western blots shown on the right. Uncropped gel images are shown in **Supplemental Fig. S10**.

Figure 4. MKRN1 stalls ribosomes at poly(A) sequences. (A) The dual fluorescence reporter harbours an N-terminal GFP, followed by a FLAG-SR-X linker and a C-terminal RFP, which are separated by P2A sites to ensure translation into three separate proteins (Juszkiewicz and Hegde 2017). The resulting GFP:RFP ratio was determined using flow cytometry. The inserted fragment K(AAA)₂₀ encodes 20 lysines by repeating the codon AAA. The starting vector without insert (K₀) served as control. Schematic ribosomes illustrate translation of the respective reporter segments. (B) Ribosomes are efficiently stalled at K(AAA)₂₀ in HEK293T cells. Median RFP:GFP ratios, normalised to K₀, are shown. Error bars represent standard deviation of the mean (s.d.m., n = 6 replicates). *P* value indicated above (paired two-tailed t-test). (C) Ribosomes fail to stall in the absence of MKRN1. HEK293T cells were transfected with control siRNA or siRNAs targeting *MKRN1* (KD1 and KD2) or *ZNF598* for 24 h, followed by transfection of the reporter plasmids for 48 h. Western blots for KDs are shown in **Supplemental Fig. S6B**. RFP and GFP signals were analysed by flow cytometry. Median RFP:GFP ratios, normalised to K₀ in control, are shown. Error bars represent s.d.m.; *P* values indicated above (paired two-tailed t-test, Benjamini-Hochberg correction, n ≥ 6 replicates; ns, not significant).

Figure 5. MKRN1 ubiquitylates ribosomal protein RPS10 and translational regulators. (A) Ubiquitin remnant profiling to compare the relative abundance of ubiquitylation sites in *MKRN1* KD2 and control HEK293T cells. Ubiquitin remnant peptides were enriched and analysed by quantitative mass spectrometry, quantifying a total of 15,528 ubiquitylation sites. 29 putative MKRN1 target sites with significantly decreased ubiquitylation upon *MKRN1* KD2 (FDR < 10%, n = 4 replicates) are highlighted and labelled with the respective protein name. Note that many proteins contain several differentially regulated ubiquitylation sites. (B) Protein interaction network of 21 proteins with putative MKRN1 ubiquitylation target sites (significantly reduced, shown in (A)). The functional interactions were obtained from the STRING and BioGrid databases and our study. Visualisation by Cytoscape. (C) Ubiquitin remnant profiling results for significantly regulated ubiquitylation sites (FDR < 10%) in proteins from network in (B). Mean and standard deviation of the mean (s.d.m., error bars) are given together with all data points. (D) Ubiquitin remnant profiling results for seven quantified ubiquitylation sites in RPS10 and RPS20. Significant changes are shown in black (FDR < 10%) and non-significant changes in grey. Representation as in (C). (E) Comparison of ubiquitylation sites in selected target proteins that are modified by ZNF598 and MKRN1 during RQC. (F) Comparison of enriched proteins from the interactomes for GFP-MKRN1^{wt} (over GFP, see **Fig. 1A**) and GFP-MKRN1^{RINGmut} (over GFP-MKRN1^{wt}, see **Supplemental Fig. S7B**) with the proteins containing MKRN1 ubiquitylation targets sites (UB, see (A)). Protein names of overlapping targets are given.

Figure 6. MKRN1 is a sensor for poly(A) sequences that stalls ribosomes to initiate ribosome-associated quality control. Proposed model of MKRN1 function: MKRN1 is positioned upstream of (premature) poly(A) tails via interaction with PABP. Ribosomes translating the open reading frame run into MKRN1 that acts as a roadblock to prohibit poly(A) translation. Upon contact with the translating ribosome, MKRN1 ubiquitylates the 40S ribosomal protein RPS10. This stalls the ribosome, causing the trailing ribosomes to collide. ZNF598 recognises the collided ribosomes and ubiquitylates ribosomal proteins to promote RQC.

Supplemental figure legends

Supplemental Figure S1. Maximum likelihood tree of Makorin orthologs with their protein domain architecture. (A) Maximum likelihood tree with 100 bootstrap replicates of selected vertebrate and invertebrate orthologs and *C. elegans* as an outgroup. Bootstrap values at each node indicate the number of replicates (out of 100) that support the local tree structure and thereby serve as confidence estimates. Protein schematics (drawn to scale) on the right depict protein domains corresponding to the following PFAM domains: RING-type zinc finger, PF13445; MKRN1 C-terminus, PF15815; CCCH zinc finger, PF15663, PF14608 and PF00642. PAM2 motifs, predicted to interact with the MLLE domain of PABP proteins (Kozlov et al. 2001) as well as the recently reported derivative PAM2L (Pohlmann et al. 2015), were added separately (see Material and methods). Abbreviated and full species names with corresponding UniProt identifiers in order of appearance: ANOGA, *Anopheles gambiae*, Q7QF83; BOVIN, *Bos taurus*, F1MF12, F6QQR5; BRAFL, *Branchiostoma floridae*, C3Y7M0; CAEEL, *Caenorhabditis elegans*, Q9N373; CANLF, *Canis lupus*, J9P921, E2RRA5, E2REH2, J9P9K3; DANRE, *Danio rerio*, Q4VBT5, Q9DFG8, A9C4A6; DROME, *Drosophila melanogaster*, Q9VP20; CHICKEN, *Gallus gallus*, Q9PTI4, F1NI93; GORGO, *Gorilla gorilla*, G3S6Y3, G3QDU4, G3RZ99; HUMAN, *Homo sapiens*, Q9UHC7, Q9H000, Q13064; IXOSC, *Ixodes scapularis*, B7QIJ9, B7Q4B2; LEPOC, *Lepisosteus oculatus*, W5NGW8, W5N9B2, W5LWJ1; MONDO, *Monodelphis domestica*, F6QPR3, F7F0I3; MOUSE, *Mus musculus*, Q9QXP6, Q9ERV1, Q60764; ORYLA, *Oryzias latipes*, H2MBR3, H2M1P4, H2LQG1; PANTR, *Pan troglodytes*, H2QVH8, H2QM29, H2Q915; RAT, *Rattus norvegicus*, A0A0G2QC40, Q5XI23, D3ZY41; XENTR, *Xenopus tropicalis*, Q6GLD9, B4F720. (B) The PAM2 motif in Makorin proteins from vertebrates (bottom, species abbreviations as in (A)) shows similarities to PAM2 in known PABP-interacting proteins from human

(top, protein names given; first amino acid position for all PAM2 motifs indicated on the left in grey). The PAM2 consensus (Kozlov et al. 2001) is given above. Positions 9, 10 and 12 within the aligned regions that are highly consistent between all aligned proteins and important for PAM2 function (Kozlov et al. 2004) are highlighted in brown. Mutations that were introduced to abrogate the function of the PAM2 motif in human MKRN1 (MKRN1^{PAM2mut}) are shown below. The corresponding UniProt identifiers are Q8IYD1, Q8NDV7, Q99700, Q9H074, Q9BPZ3 (known PABP-interacting proteins from human), Q9UHC7, H2QVH8, G3S6Y3, J9P921, E2RRA5, F1MF12, Q5XI23, Q9QXP6, Q9PTI4, F6QPR3, W5NGW8, Q4VBT5, H2MBR3 (Makorin orthologs from vertebrates). (C) The closest Makorin orthologs in *Saccharomyces cerevisiae* lack RING domain and PAM2 motif. Domain architecture of Yth1p and Lee1p, which were detected as closest orthologs by HaMStR-OneSeq (Ebersberger et al. 2014), but were not considered as orthologs due to low FAS scores (0,59 and 0,60, respectively). The annotated PFAM domains are CCCH zinc finger, PF15663, PF00642, PF16131.

Supplemental Figure S2. MKRN1 interacts with translational regulators and other RBPs. (A) Overlap of the 53 significant interaction partners of GFP-MKRN1^{wt} in human HEK293T cells with previously published interactors of MKRN1 in mouse embryonic stem cells (mESC) (Cassar et al. 2015). (B) GO terms enriched for the 53 MKRN1 interactors. *P* values (modified Fisher exact test, Benjamini-Hochberg correction) are depicted for all significant GO terms (corrected *P* value < 0.05) for Biological Process, Molecular Function and Cellular Compartment, together with the number of interactors associated with the respective term. (C) Reciprocal APs show that MKRN1 interacts with PABPC1, ELAVL1 and IGF2BP1 independently of RNA. AP with GFP-PABPC1, GFP-ELAVL1 and GFP-IGF2BP1 as baits were performed from HEK293T cells in the

presence or absence of RNase A and T1. Bait proteins and endogenous MKRN1 were detected by Western blots (replicate 1). Different exposure times (exp.) for MKRN1 are shown for GFP-ELAVL1 and GFP-IGF2BP1 APs. Quantifications (fold changes of the MKRN1 signal over empty vector (EV)) of three replicates are shown on the right. Replicates 2 and 3, and uncropped gel images are shown in **Supplemental Fig. S9D-F**.

Supplemental Figure S3. Signal-over-background transformation allows to estimate MKRN1 binding strength. (A-C) Raw iCLIP signal before signal-over-background transformation. (A) Scatter plots show pairwise comparisons of crosslink events per binding site in three replicate MKRN1 iCLIP experiments. Pearson correlation coefficients (r) and associated P values are given. (B) Density plots depict the distribution of crosslink events per binding site in the three replicate experiments. Shades of blue indicate 20% quantiles; top 20% of binding sites with highest counts are denoted by a dashed line. (C) Raw iCLIP counts are strongly influenced by the expression level of the underlying gene. MKRN1-bound genes were stratified into 50 bins with increasing expression (using the total number of MKRN1 crosslink events within the 3' UTR as a proxy of a gene's expression level). Shown is the average number of crosslink events per binding site for all binding sites in each bin. Dashed line denotes median across all bins. (D-F) Signal-over-background (SOB) values allow to correct for expression-level differences. (D) Pairwise comparison of SOB values for the three MKRN1 iCLIP replicate experiments. Scatter plots as in (A). (E) Distribution of SOB values in the three replicates. Density plots as in (B). Shades of blue indicate 20% quantiles. Dashed lines denote the top 20% MKRN1 binding sites with strongest binding that were used for the analyses in **Fig. 2B** and **Supplemental Fig. S4A**. (F)

SOB values are independent of the expression level of the underlying gene. Average SOB values for all binding sites in each expression bin are shown as in (C).

Supplemental Figure S4. MKRN1 binds upstream of long A-stretches. (A) Binding sites with associated A-stretches show stronger MKRN1 binding. Boxplot compares the SOB values of MKRN1 binding sites in 3' UTRs with and without associated A-stretches. Number of binding sites indicated inside box. (B) Heatmap representation of 1,412 non-overlapping A-stretches at MKRN1 binding sites, sorted by increasing length (8-30 nt). Only A's are coloured. (C) MKRN1 binding site strength (signal-over-background, SOB) increases with length of associated A-stretch. Mean and standard deviation of MKRN1 binding sites associated with A-stretches of increasing length (x-axis). MKRN1 binding sites without associated A-stretches are shown for comparison on the left. Number of binding sites in each category indicated as barchart above. (D) The top 20% MKRN1 binding sites show a strong RNA binding preference for AAAA. Scatter plot compares the frequency of 4-mers within the 9-nt MKRN1 binding sites and flanking 40-nt windows for the top 20% and bottom 20% MKRN1 binding sites (according to SOB). 4-mer frequencies are displayed as z-scores based on background distribution from binding site permutations.

Supplemental Figure S5. Interaction with PABP is required for MKRN1 RNA binding. (A,B) UV crosslinking experiments to measure the RNA binding capacity of GFP-MKRN1^{wt} and GFP-MKRN1^{PAM2mut}. Autoradiographs (top) and Western blots (bottom) show GFP-MKRN1/RNA complexes and GFP-MKRN1 protein, respectively, in the eluates from replicates 2 (with 4SU and UV crosslinking at 365 nm) (A) and 3 (with conventional UV crosslinking at 254 nm) (B). For calibration, input samples for GFP-

MKRN1^{wt} were diluted to 75%, 50% and 25% prior to GFP AP. Note that samples were loaded in different order in (B). Quantifications are given below. Uncropped gel images are shown in **Supplemental Fig. S10**.

Supplemental Figure S6. MKRN1 is required to stall ribosomes at K(AAA)₂₀ in reporter assays. (A) Translation of dual fluorescence reporter plasmids was assessed by flow cytometry upon *MKRN1* and/or *ZNF598* KD. Median RFP:GFP ratios (normalised to K₀ in control KD) are shown for the reporter plasmids K₀, K(AAA)₁₂, K(AAA)₂₀, and R(CG A)₁₀. Error bars represent standard deviation of the mean (s.d.m., n ≥ 6 replicates; paired two-tailed t-test, Benjamini-Hochberg correction). Density plot of median RFP:GFP ratios of one replicate experiment with K(AAA)₂₀ with control or *MKRN1* KD (two independent siRNAs, KD1 and KD2) or *ZNF598* is shown on the right. (B) KDs of *MKRN1* and *ZNF598* were assessed by Western blot (n = 3 replicates). Black arrowhead indicates ZNF598. Replicates 2 and 3, and uncropped gel images are shown in **Supplemental Fig. S11A,B**. (C) *MKRN1* KD2 also reduces *MKRN2* levels. *MKRN1* KD1 and KD2 were performed for 72 h. Expression levels of *MKRN1* and *MKRN2* were assessed in relation to *β-actin* levels by qPCR in *MKRN1* KD (siRNA 1 and 2) and control KD. Error bars indicate s.d.m. (n = 2 replicates). (D,E) Cross-regulation of MKRN1 and ZNF598. (D) *MKRN1* KD1 reduces endogenous ZNF598 protein levels. Effect of *MKRN1* KD (KD1, siRNA 1 and KD2, siRNA 2) and *ZNF598* KD for 72 h was assessed by Western blot for endogenous MKRN1 and ZNF598. Quantifications depict MKRN1 or ZNF598 expression levels in *MKRN1* or *ZNF598* KD over control KD condition, normalised to tubulin levels (n = 3 replicates). Replicates 2 and 3, and uncropped gel images are shown in **Supplemental Fig. S11C,D**. (E) *ZNF598* overexpression reduces MKRN1 protein levels. Effect of *ZNF598* and *MKRN1*

(wt and mutants) overexpression was tested after 48 h. Quantification as in (D).
Uncropped gel images for all replicates are shown in **Supplemental Fig. S11E,F**.

Supplemental Figure S7. Interactome of GFP-MKRN1^{RINGmut} reveals putative ubiquitylation substrates. Experiments were performed using SILAC-based MS. Asymmetrical z-scores of combined SILAC ratios (n = 3 replicates) are shown. Proteins are detected in at least two out of three replicates. (A) Protein interactome of GFP-MKRN1^{RINGmut} in HEK293T cells analysed by quantitative mass spectrometry. Combined SILAC ratios (n = 3 replicates) after z-score normalisation are plotted against log₁₀-transformed intensities. 1,097 protein groups were quantified in at least two out of three replicates (**Supplemental Table S1**). MKRN1 and interesting candidate ubiquitylation targets are highlighted. (B) Quantitative comparison of the interactome of GFP-MKRN1^{wt} and GFP-MKRN1^{RINGmut} shows that potential ubiquitylation candidates identified in (A) are enriched in GFP-MKRN1^{RINGmut} over GFP-MKRN1^{wt}. Comparison reveals 137 proteins to be significantly enriched (MKRN1^{RINGmut} over MKRN1^{wt} with FDR < 5% and MKRN1^{wt}/GFP z-score > 1). Combined ratios of three replicates are shown in a scatter plot. Only proteins detected in at least two out of three replicates are shown. Highlighting as in (A).

Supplemental Figure S8. GO term analysis of MKRN1 ubiquitylation targets and proteome analysis upon *MKRN1* KD. (A) GO terms enriched for the 21 MKRN1 ubiquitylation targets. Corrected *P* values (modified Fisher exact test, Benjamini-Hochberg correction) are depicted for all significant GO terms (corrected *P* value < 0.05) for Biological Process (BP), Molecular Function (MF) and Cellular Compartment (CC), together with the number of ubiquitylation targets associated with the respective

term. (B) Proteome analysis of *MKRN1* KD in HEK293T cells analysed by quantitative mass spectrometry. Log₂-transformed, combined normalised SILAC ratios (n = 3 replicates) are plotted against log₁₀-transformed intensities. 6,425 protein groups were quantified in at least one out of three replicate experiments (**Supplemental Table S4**). Selected ubiquitylation targets of MKRN1 are highlighted.

Supplemental Figure S9. Images of full membranes and different exposure times (exp.) for Western blot analyses in **Fig. 1C** and **Supplemental Fig. S2C** in the presence or absence of RNase A and T1. (A-C) PABP interacts with MKRN1^{wt} and MKRN1^{RINGmut} but not MKRN1^{PAM2mut}. Western blot analysis was performed with antibodies against PABPC1/3 and GFP. Images of full membranes and different exposure (exp.) times for both antibodies are shown for replicate 1 (A) which is presented in **Fig. 1C**, as well as replicates 2 (B) and 3 (C). Black and blue arrowheads indicate GFP-MKRN1 and PABPC1/3, respectively. (D-F) Endogenous MKRN1 interacts with GFP-PABPC1 independent of RNA. Western blot analysis was performed with antibodies against MKRN1 and GFP. Images of full membranes and different exposure times for both antibodies are shown for replicate 1 (D) which is presented in **Supplemental Fig. S2C**, as well as replicates 2 (E) and 3 (F). Black and blue arrowheads indicate MKRN1 and GFP-PABPC1, replicates. (G-I) Endogenous MKRN1 interacts with GFP-ELAVL1 independent of RNA. Western blot analysis was performed with antibodies against MKRN1 and GFP. Images of full membranes and different exposure times for both antibodies are shown for replicate 1 (G) which is presented in **Supplemental Fig. S2C**, as well as replicates 2 (H) and 3 (I). (J-L) Endogenous MKRN1 interacts with GFP-IGF2BP1 independent of RNA. Western blot analysis was performed with antibodies against MKRN1 and GFP. Images of full

membranes and different exposure times for both antibodies are shown for replicate 1 (J) which is presented in **Supplemental Fig. S2C**, as well as replicates 2 (K) and 3 (L).

Supplemental Figure S10. Images of full membranes of autoradiographs and Western blot analyses in **Fig. 3D** (replicate 1) and **Supplemental Fig. S5** (replicates 2 and 3). UV crosslinking experiments to measure the RNA binding capacity of GFP-MKRN1^{wt} and GFP-MKRN1^{PAM2mut}. Autoradiographs (A, left; B, top) and Western blots (A, right; B, bottom) show GFP-MKRN1/RNA complexes and GFP-MKRN1 protein, respectively, in the eluates from replicates 1 and 2 (with 4SU and UV crosslinking at 365 nm) (A) and 3 (with conventional UV crosslinking at 254 nm) (B). (B) Images of full membranes of Western blot analyses with both antibodies are shown for replicate 3 (B).

Supplemental Figure S11. Images of full membranes and different exposure (exp.) times for Western blot analyses in **Supplemental Fig. S6B,D,E**. (A,B) KDs of *MKRN1* and *ZNF598* assessed by Western blot (n = 3 replicates) from **Supplemental Fig. S6B**. Western blot analysis was performed with antibodies against MKRN1, ZNF598, and tubulin. Black and blue arrowheads indicate MKRN1 (53 kDa) and ZNF598 (99 kDa), respectively. Uncropped gel images of replicates 1 and 2 (A) and 3 (B). (C,D) Images of full membranes are shown for cross-regulation between *MKRN1* and *ZNF598* KD from **Supplemental Fig. S6D**. *MKRN1* KD1 reduces endogenous ZNF598 protein levels. Western blot analysis was performed with antibodies against MKRN1, ZNF598, and tubulin. Coloured arrowheads as in (A). Uncropped gel images of replicate 1 (C) and replicates 2 and 3 (D). (E,F) Images of full membranes are shown

for cross-regulation of *MKRN1* and *ZNF598* overexpression (OE) from **Supplemental Fig. S6E**. *ZNF598* OE reduces MKRN1 protein levels. Western blot analysis was performed with antibodies against MKRN1, ZNF598, and tubulin. Black arrowheads indicate MKRN1. Images of full membranes and different exposure times (exp.) for both antibodies are shown for replicates 1, 2 (*E*), and 3 (*F*). Note the opposite order of replicates 1 and 2 (2 left, 1 right) in (*E*).

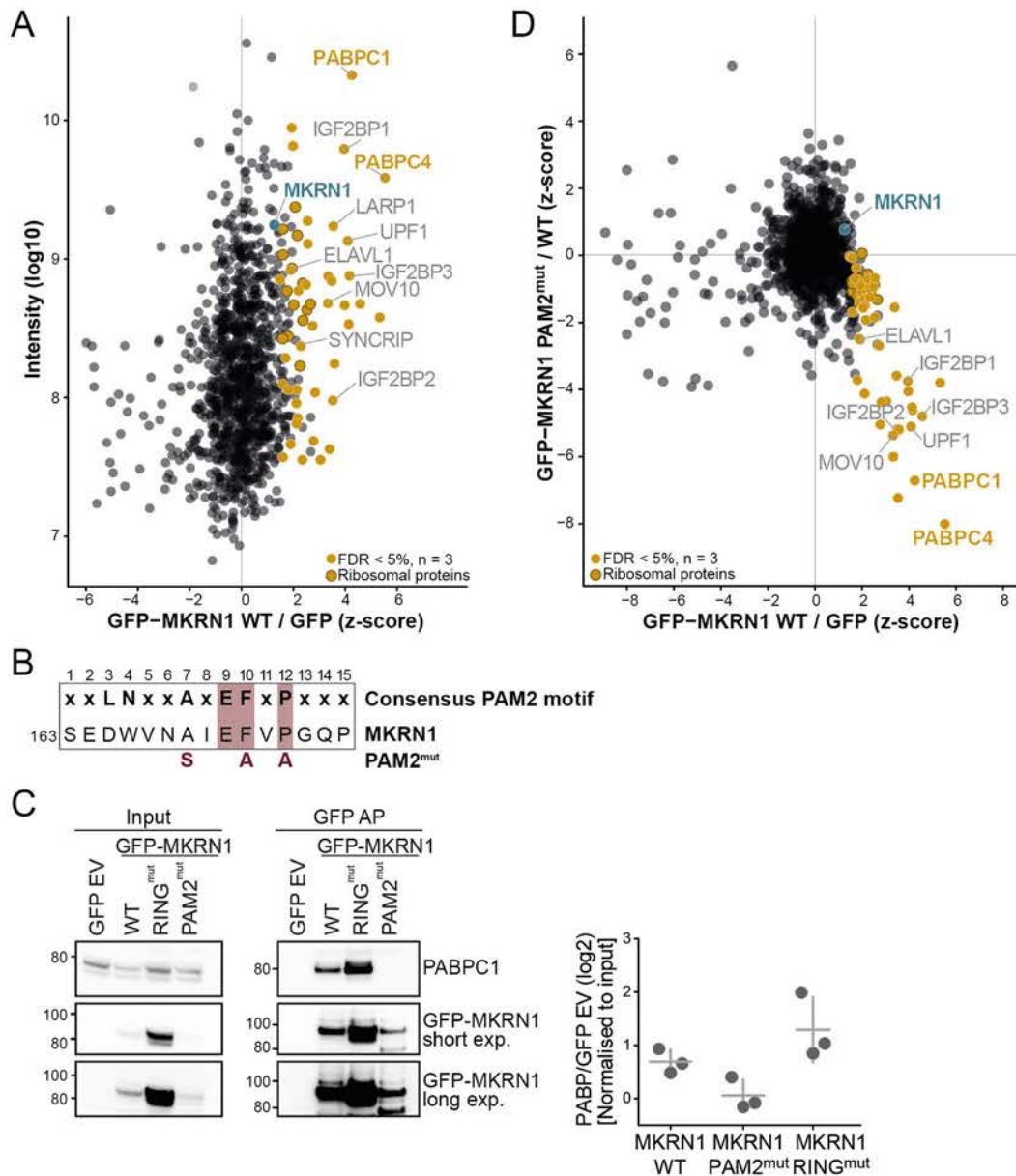


Figure 1. MKRN1 interacts with PABP and other regulators of translation and RNA stability. (A) Protein interactome of GFP-MKRN1^{WT} in HEK293T cells analysed by quantitative MS-based proteomics. Combined SILAC ratios (n = 3 replicates) after z-score normalisation are plotted against \log_{10} -transformed intensities. 1,100 protein groups were quantified in at least two out of three replicate experiments. MKRN1 and significant interactors are highlighted (FDR < 5%). (B) A PAM2 motif similar to the previously reported consensus (shown on top; Supplemental Fig. S1B) (Albrecht and Lengauer 2004) is present in MKRN1 (first amino acid position indicated on the left). Introduced mutations in MKRN1^{PAM2mut} are indicated in red below. Relevant positions are highlighted (Supplemental Fig. S1B). (C) Endogenous PABP interacts with MKRN1^{WT} and MKRN1^{RINGmut}, but not with MKRN1^{PAM2mut}. Western blots for endogenous PABPC1 and GFP (two exposure times, exp.) after AP of GFP-MKRN1 (wt and mutants). Ratios of PABP signal (normalised to input) in GFP-MKRN1 APs over control (GFP empty vector, EV) are shown on the right. Replicates 2, 3, and uncropped gel images are shown in Supplemental Fig. S9A-C. (D) Quantitative comparison of the interactomes of GFP-MKRN1^{WT} and GFP-MKRN1^{PAM2mut} shows that PABP and several other interactors are lost upon PAM2 mutation. Combined ratios of three replicates are shown in a scatter plot. Only proteins detected in at least two out of three replicates are shown. MKRN1^{WT} significant interactors (from A) are highlighted as in (A) (FDR < 5% in GFP-MKRN1^{WT}).

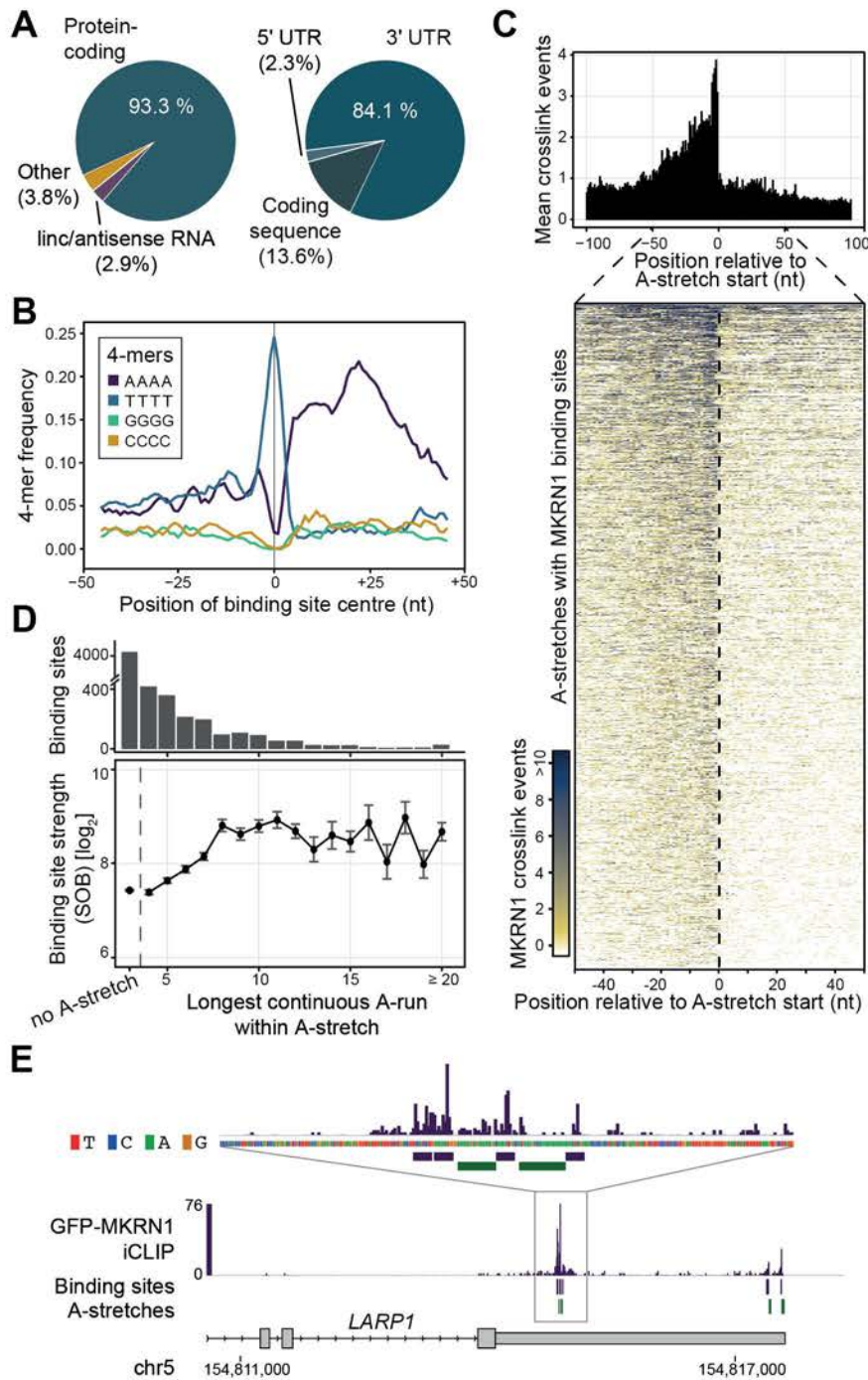


Figure 2. MKRN1 binds upstream of A-stretches in 3' UTRs. (A) MKRN1 predominantly binds in the 3' UTR of protein-coding genes. Piecharts summarising the distribution of MKRN1 binding sites to different RNA biotypes (7,331 binding sites, left) and different regions within protein-coding transcripts (6,913 binding sites, right). (B) MKRN1 binding sites display a downstream enrichment of AAAA homopolymers. Frequency per nucleotide (nt) for four homopolymeric 4-mers in a 101-nt window around the midpoints of the top 20% MKRN1 binding sites (according to signal-over-background; see Material and methods). (C) MKRN1 crosslink events accumulate upstream of A-stretches. Metaprofile (top) shows the mean crosslink events per nt in a 201-nt window around the start position of 1,412 MKRN1-associated A-stretches in 3' UTRs. Heatmap visualisation (bottom) displays crosslink events per nt (see colour scale) in a 101-nt window around the MKRN1-associated A-stretches. (D) MKRN1 binding site strength (signal-over-background, SOB) increases with length of longest continuous run of A's (LCA) within the A-stretch. Mean and standard deviation of MKRN1 binding sites associated with A-stretches harbouring LCAs of increasing length (x-axis). MKRN1 binding sites without associated A-stretches are shown for comparison on the left. Number of binding sites in each category indicated as barchart above. (E) MKRN1 binds upstream of A-stretches in the 3' UTR of the *LARP1* gene. Genome browser view of GFP-MKRN1 iCLIP data showing crosslink events per nt (merged replicates, turquoise) together with binding sites (lilac) and associated A-stretches (dark green).

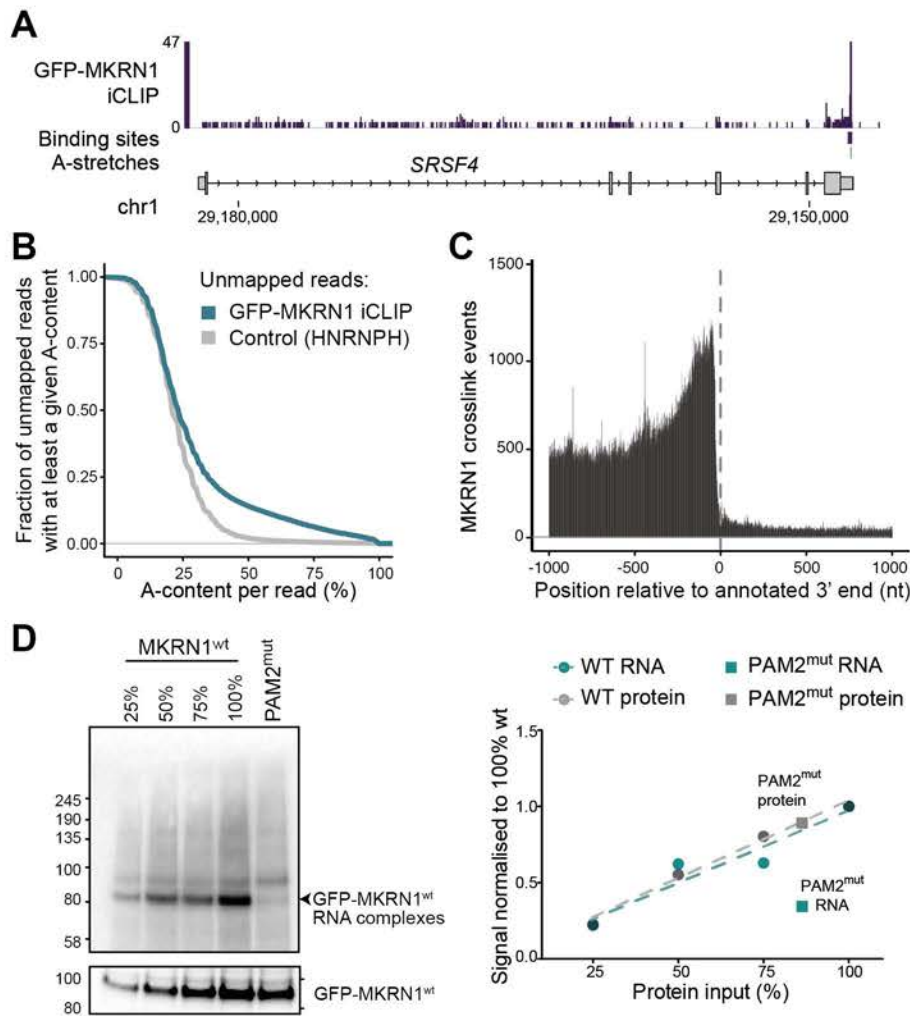
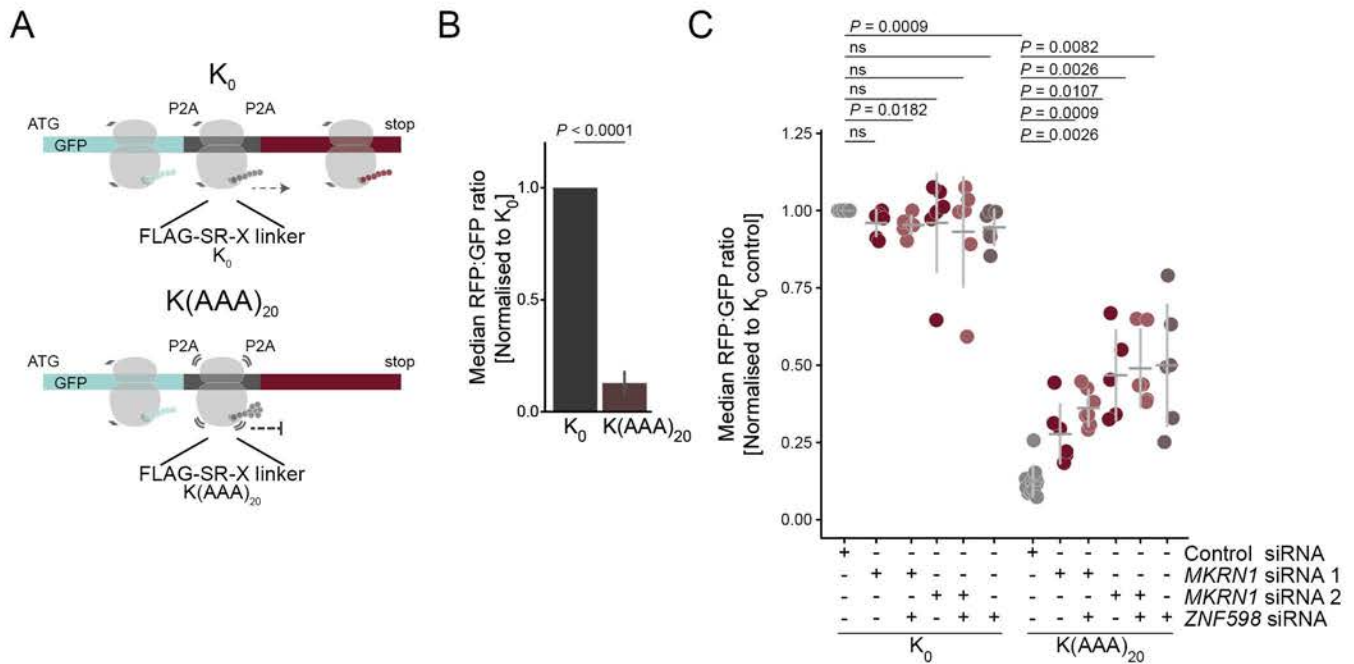


Figure 3. MKRN1 binds at poly(A) tails. (A) MKRN1 binds at the annotated transcript 3' end in the *SRSF4* gene. Genome browser view as in Fig. 2E. (B) Unmapped MKRN1 iCLIP reads display increased A-content (more than half of all nucleotides in the read), evidencing poly(A) tail binding. Cumulative fraction of iCLIP reads (y-axis, merged replicates) that could not be mapped to the human genome (see Materials and methods) and show at least a given A-content (x-axis). iCLIP data for the unrelated RBP HNRNPH (Braun et al. 2018) are shown for comparison. (C) MKRN1 crosslink events increase towards 3' UTR ends. Metaprofile shows the sum of crosslink events per nt in a 2001-nt window around annotated transcript 3' ends of transcripts with >1 kb 3' UTRs (n = 63,030). (D) Overall RNA binding of MKRN1 is strongly reduced when abrogating PABP interaction. Autoradiograph (left) of UV crosslinking experiments (replicate 1, with 4SU and UV crosslinking at 365 nm; replicates 2 and 3 in Supplemental Fig. S5) comparing GFP-MKRN1^{PAM2mut} with GFP-MKRN1^{wt} at different dilution steps for calibration. Quantification of radioactive signal of protein-RNA complexes and corresponding Western blots shown on the right. Uncropped gel images are shown in Supplemental Fig. S10.



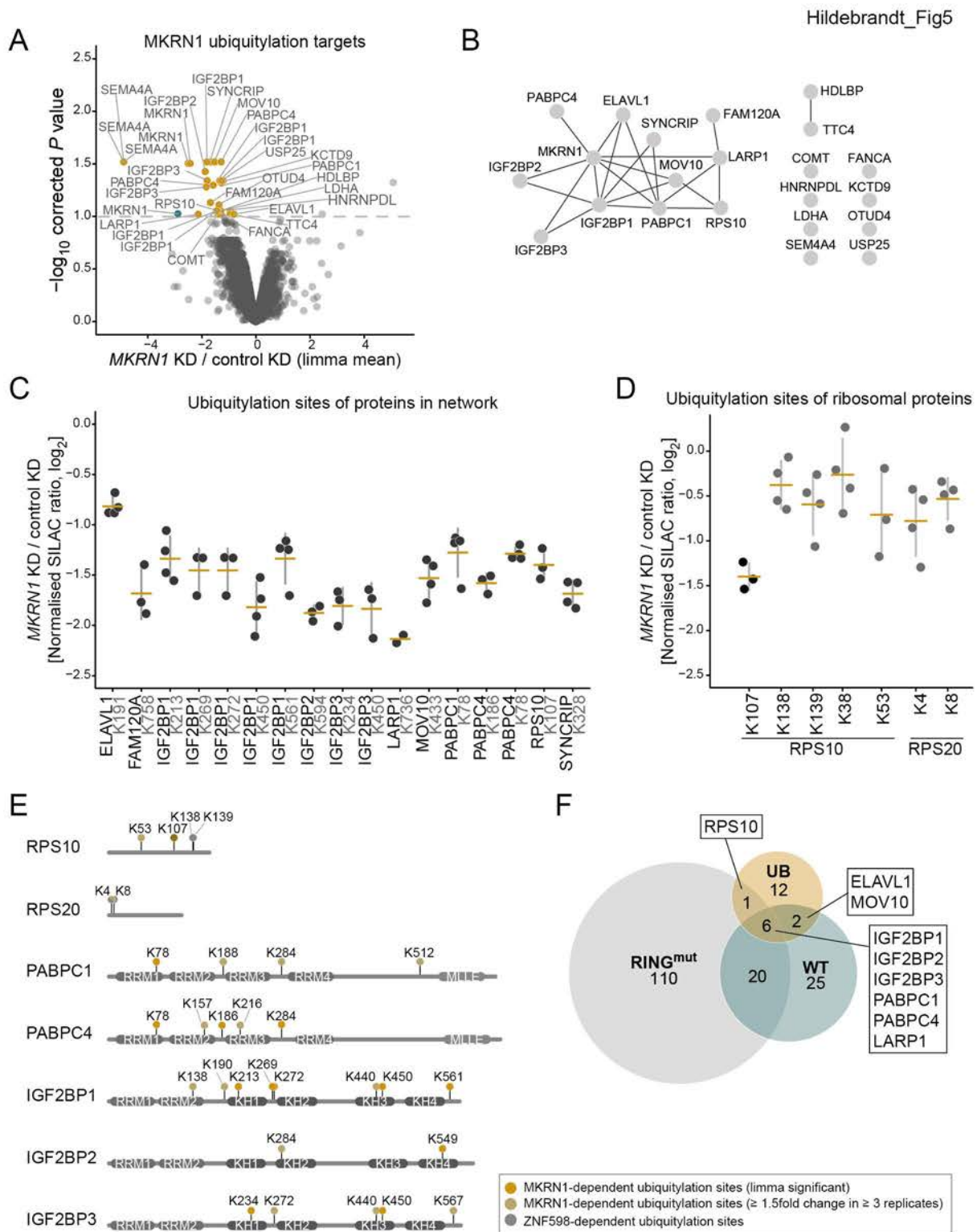


Figure 5. MKRN1 ubiquitylates ribosomal protein RPS10 and translational regulators. (A) Ubiquitin remnant profiling to compare the relative abundance of ubiquitylation sites in *MKRN1* KD2 and control HEK293T cells. Ubiquitin remnant peptides were enriched and analysed by quantitative mass spectrometry, quantifying a total of 15,528 ubiquitylation sites. 29 putative MKRN1 target sites with significantly decreased ubiquitylation upon *MKRN1* KD2 (FDR < 10%, n = 4 replicates) are highlighted and labelled with the respective protein name. Note that many proteins contain several differentially regulated ubiquitylation sites. (B) Protein interaction network of 21 proteins with putative MKRN1 ubiquitylation target sites (significantly reduced, shown in (A)). The functional interactions were obtained from the STRING and BioGrid databases and our study. Visualisation by Cytoscape. (C) Ubiquitin remnant profiling results for significantly regulated ubiquitylation sites (FDR < 10%) in proteins from network in (B). Mean and standard deviation of the mean (s.d.m., error bars) are given together with all data points. (D) Ubiquitin remnant profiling results for seven quantified ubiquitylation sites in RPS10 and RPS20. Significant changes are shown in black (FDR < 10%) and non-significant changes in grey. Representation as in (C). (E) Comparison of ubiquitylation sites in selected target proteins that are modified by ZNF598 and MKRN1 during RQC. (F) Comparison of enriched proteins from the interactomes for GFP-MKRN1^{wt} (over GFP, see Fig. 1A) and GFP-MKRN1^{RINGmut} (over GFP-MKRN1^{wt}, see Supplemental Fig. S7B) with the proteins containing MKRN1 ubiquitylation targets sites (UB, see (A)). Protein names of overlapping targets are given.

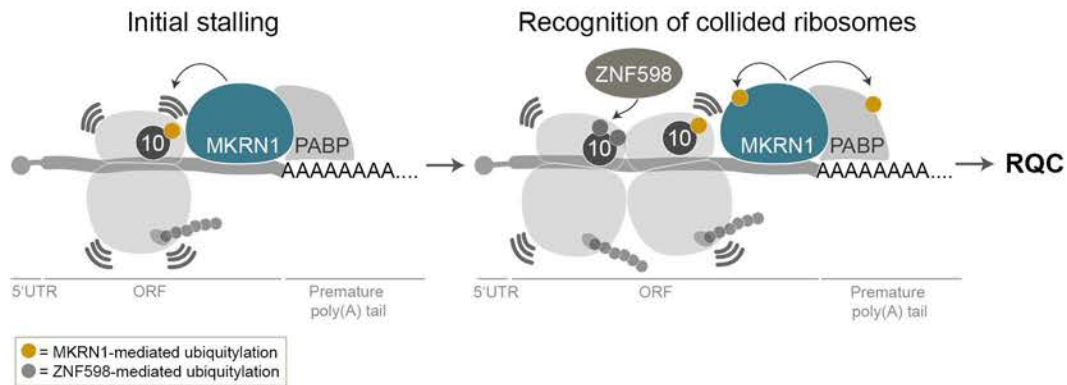
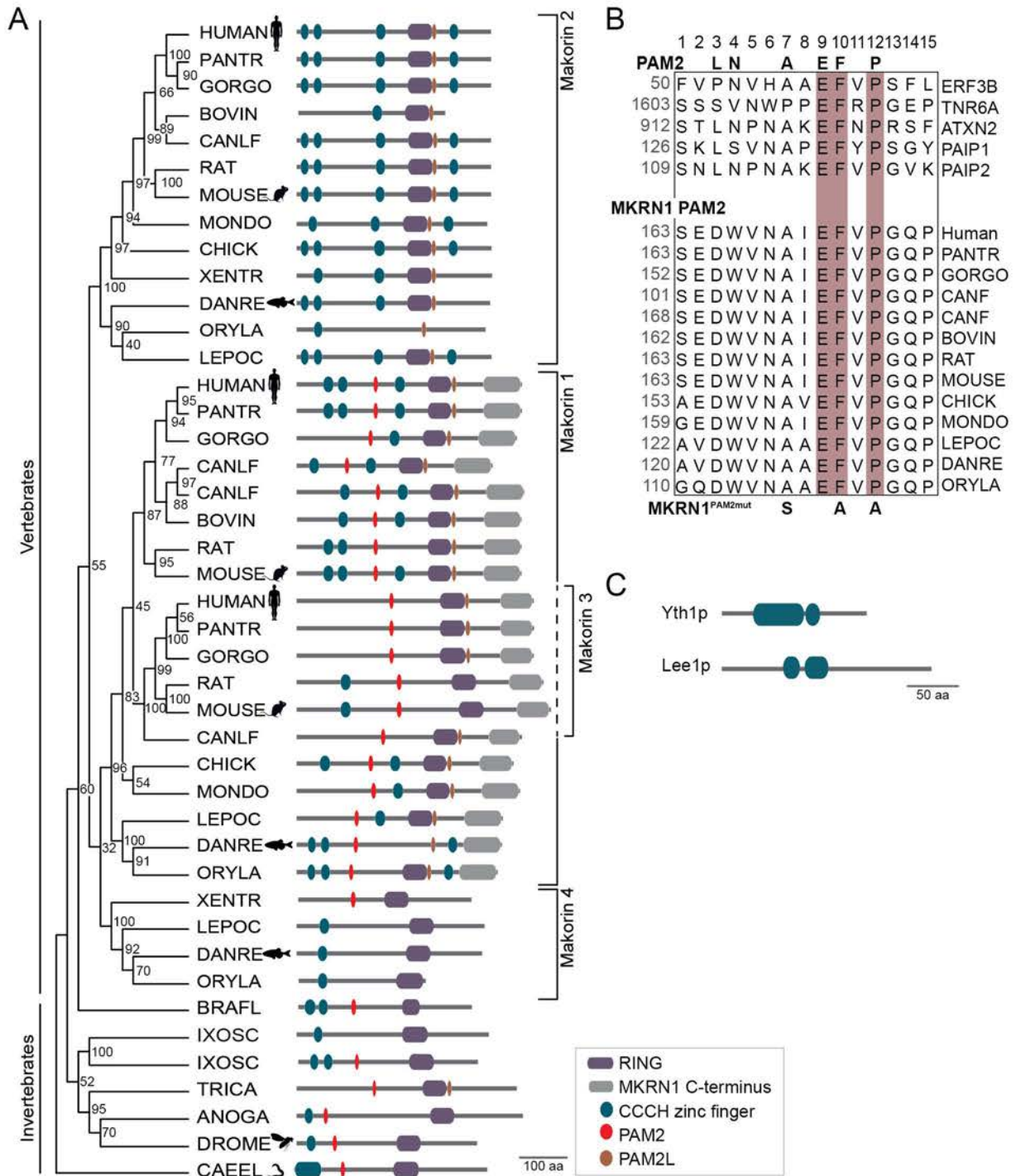
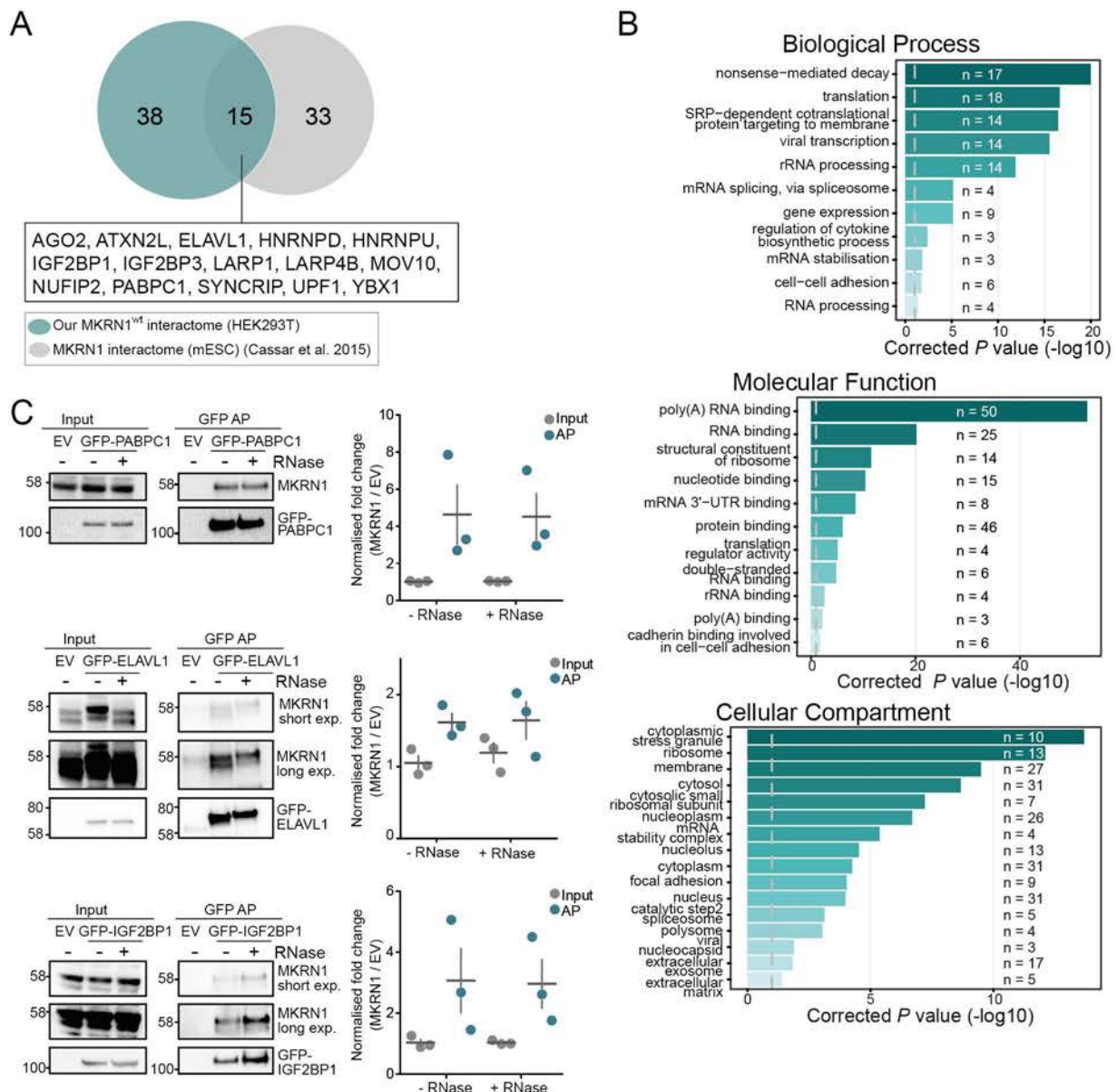


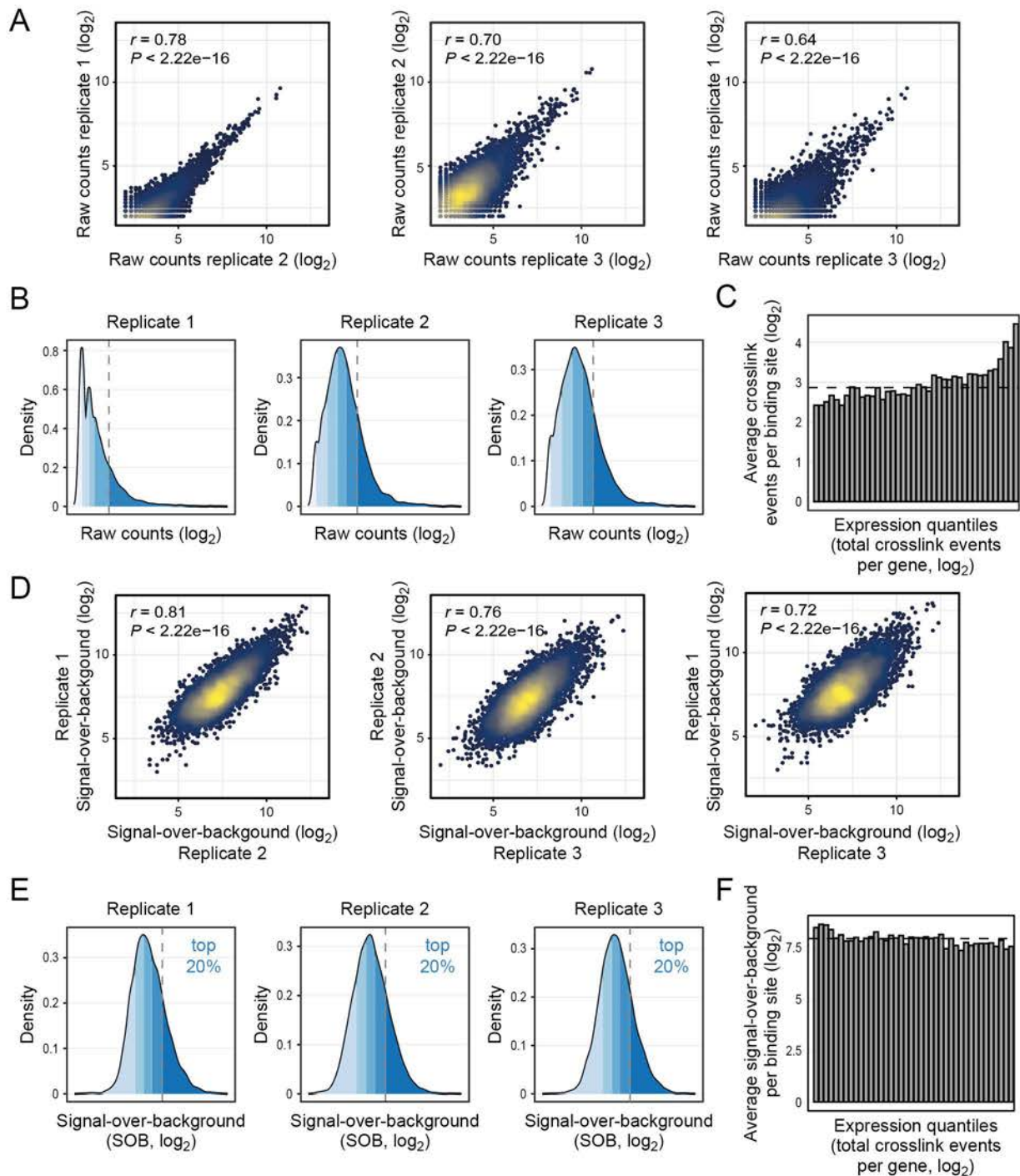
Figure 6. MKRN1 is a sensor for poly(A) sequences that stalls ribosomes to initiate ribosome-associated quality control. Proposed model of MKRN1 function: MKRN1 is positioned upstream of (premature) poly(A) tails via interaction with PABP. Ribosomes translating the open reading frame run into MKRN1 that acts as a roadblock to prohibit poly(A) translation. Upon contact with the translating ribosome, MKRN1 ubiquitylates the 40S ribosomal protein RPS10. This stalls the ribosome, causing the trailing ribosomes to collide. ZNF598 recognises the collided ribosomes and ubiquitylates ribosomal proteins to promote RQC.



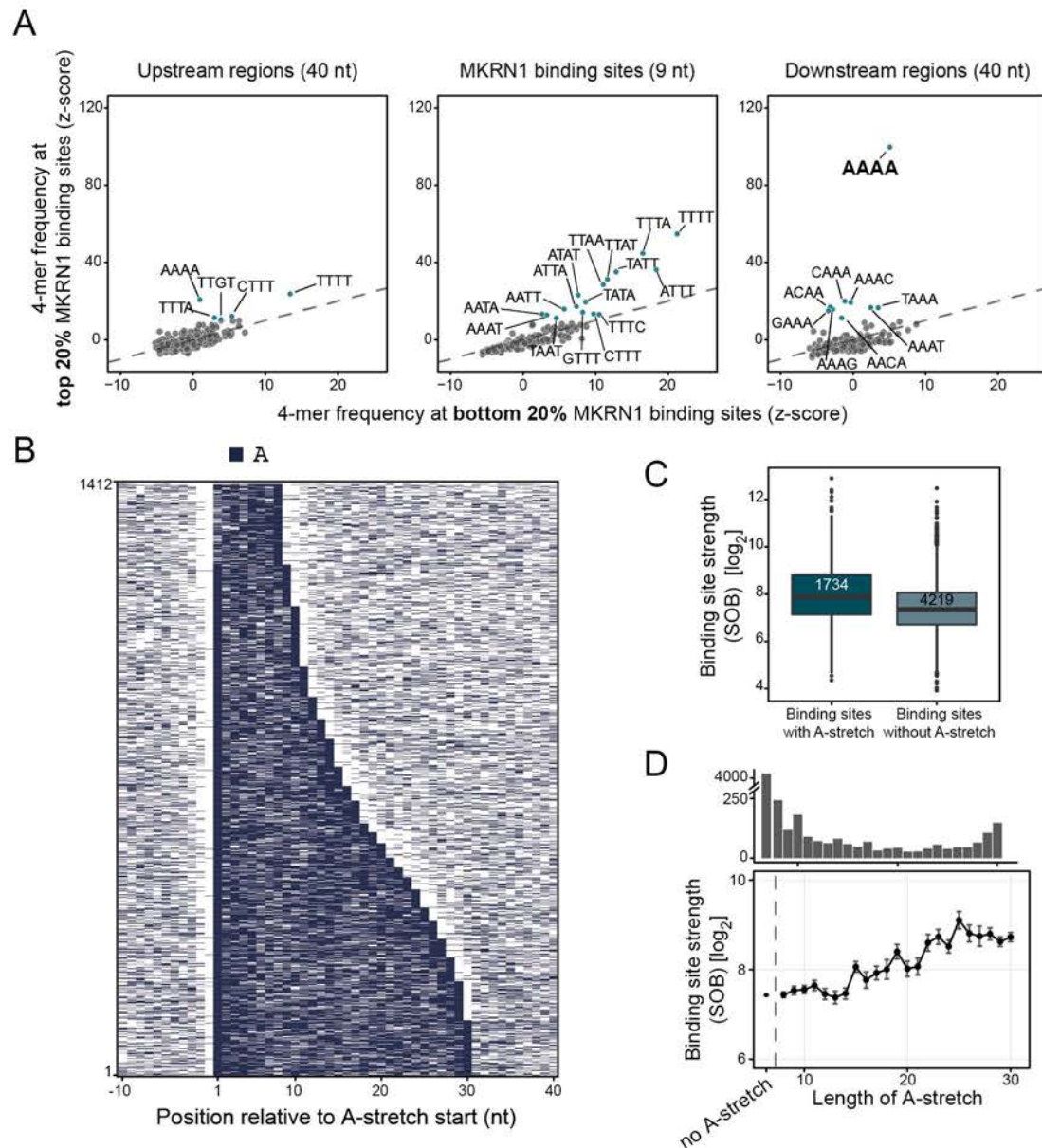
Supplemental Figure S1. Maximum likelihood tree of Makorin orthologs with their protein domain architecture. (A) Maximum likelihood tree with 100 bootstrap replicates of selected vertebrate and invertebrate orthologs and *C. elegans* as an outgroup. Bootstrap values at each node indicate the number of replicates (out of 100) that support the local tree structure and thereby serve as confidence estimates. Protein schematics (drawn to scale) on the right depict protein domains corresponding to the following PFAM domains: RING-type zinc finger, PF13445; MKRN1 C-terminus, PF15815; CCCH zinc finger, PF15663, PF14608 and PF00642. PAM2 motifs, predicted to interact with the MLE domain of PABP proteins (Kozlov et al. 2001) as well as the recently reported derivative PAM2L (Pohlmann et al. 2015), were added separately (see Material and methods). Abbreviated and full species names with corresponding UniProt identifiers in order of appearance: ANOGA, *Anopheles gambiae*, Q7QF83; BOVIN, *Bos taurus*, F1MF12, F6QQR5; BRAFL, *Branchiostoma floridae*, C3Y7M0; CAEEL, *Caenorhabditis elegans*, Q9N373; CANLF, *Canis lupus*, J9P921, E2RRA5, E2REH2, J9P9K3; DANRE, *Danio rerio*, Q4VBT5, Q9DFG8, A9C4A6; DROME, *Drosophila melanogaster*, Q9VP20; CHICKEN, *Gallus gallus*, Q9PT14, F1NI93; GORGO, *Gorilla gorilla*, G3S6Y3, G3QDU4, G3RZ99; HUMAN, *Homo sapiens*, Q9UHC7, Q9H000, Q13064; IXOSC, *Ixodes scapularis*, B7QIJ9, B7Q4B2; LEPOC, *Lepisosteus oculatus*, W5NGW8, W5N9B2, W5LWJ1; MONDO, *Monodelphis domestica*, F6QPR3, F7F0I3; MOUSE, *Mus musculus*, Q9QXP6, Q9ERV1, Q60764; ORYLA, *Oryzias latipes*, H2MBR3, H2M1P4, H2LQG1; PANTR, *Pan troglodytes*, H2QVH8, H2QM29, H2Q915; RAT, *Rattus norvegicus*, A0A0G2QC40, Q5XI23, D3ZY41; XENTR, *Xenopus tropicalis*, Q6GLD9, B4F720. (B) The PAM2 motif in Makorin proteins from vertebrates (bottom, species abbreviations as in (A)) shows similarities to PAM2 in known PABP-interacting proteins from human (top, protein names given; first amino acid position for all PAM2 motifs indicated on the left in grey). The PAM2 consensus (Kozlov et al. 2001) is given above. Positions 9, 10 and 12 within the aligned regions that are highly consistent between all aligned proteins and important for PAM2 function (Kozlov et al. 2004) are highlighted in brown. Mutations that were introduced to abrogate the function of the PAM2 motif in human MKRN1 (MKRN1^{PAM2mut}) are shown below. The corresponding UniProt identifiers are Q81YD1, Q8NDV7, Q99700, Q9H074, Q9BPZ3 (known PABP-interacting proteins from human), Q9UHC7, H2QVH8, G3S6Y3, J9P921, E2RRA5, F1MF12, Q5XI23, Q9QXP6, Q9PT14, F6QPR3, W5NGW8, Q4VBT5, H2MBR3 (Makorin orthologs from vertebrates). (C) The closest Makorin orthologs in *Saccharomyces cerevisiae* lack RING domain and PAM2 motif. Domain architecture of Yth1p and Lee1p, which were detected as closest orthologs by HaMStR-OneSeq (Ebersberger et al. 2014), but were not considered as orthologs due to low FAS scores (0,59 and 0,60, respectively). The annotated PFAM domains are CCCH zinc finger, PF15663, PF00642, PF16131.



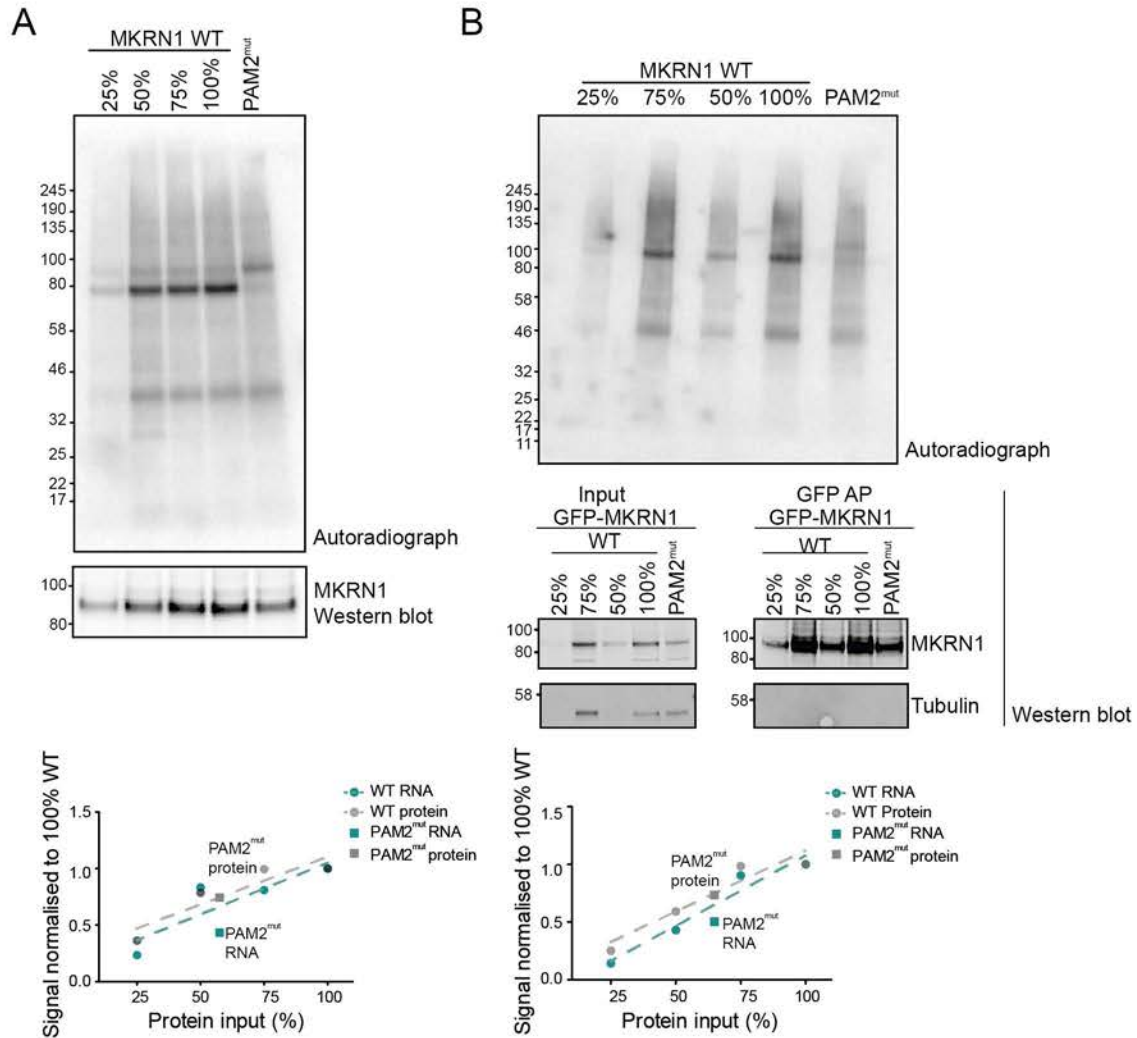
Supplemental Figure S2. MKRN1 interacts with translational regulators and other RBPs. (A) Overlap of the 53 significant interaction partners of GFP-MKRN1^{wt} in human HEK293T cells with previously published interactors of MKRN1 in mouse embryonic stem cells (mESC) (Cassar et al. 2015). (B) GO terms enriched for the 53 MKRN1 interactors. *P* values (modified Fisher exact test, Benjamini-Hochberg correction) are depicted for all significant GO terms (corrected *P* value < 0.05) for Biological Process, Molecular Function and Cellular Compartment, together with the number of interactors associated with the respective term. (C) Reciprocal APs show that MKRN1 interacts with PABPC1, ELAVL1 and IGF2BP1 independently of RNA. AP with GFP-PABPC1, GFP-ELAVL1 and GFP-IGF2BP1 as baits were performed from HEK293T cells in the presence or absence of RNase A and T1. Bait proteins and endogenous MKRN1 were detected by Western blots (replicate 1). Different exposure times (exp.) for MKRN1 are shown for GFP-ELAVL1 and GFP-IGF2BP1 APs. Quantifications (fold changes of the MKRN1 signal over empty vector (EV)) of three replicates are shown on the right. Replicates 2 and 3, and uncropped gel images are shown in Supplemental Fig. S9D-F.



Supplemental Figure S3. Signal-over-background transformation allows to estimate MKRN1 binding strength. (A-C) Raw iCLIP signal before signal-over-background transformation. (A) Scatter plots show pairwise comparisons of crosslink events per binding site in three replicate MKRN1 iCLIP experiments. Pearson correlation coefficients (r) and associated P values are given. (B) Density plots depict the distribution of crosslink events per binding site in the three replicate experiments. Shades of blue indicate 20% quantiles; top 20% of binding sites with highest counts are denoted by a dashed line. (C) Raw iCLIP counts are strongly influenced by the expression level of the underlying gene. MKRN1-bound genes were stratified into 50 bins with increasing expression (using the total number of MKRN1 crosslink events within the 3' UTR as a proxy of a gene's expression level). Shown is the average number of crosslink events per binding site for all binding sites in each bin. Dashed line denotes median across all bins. (D-F) Signal-over-background (SOB) values allow to correct for expression-level differences. (D) Pairwise comparison of SOB values for the three MKRN1 iCLIP replicate experiments. Scatter plots as in (A). (E) Distribution of SOB values in the three replicates. Density plots as in (B). Shades of blue indicate 20% quantiles. Dashed lines denote the top 20% MKRN1 binding sites with strongest binding that were used for the analyses in Fig. 2B and Supplemental Fig. S4A. (F) SOB values are independent of the expression level of the underlying gene. Average SOB values for all binding sites in each expression bin are shown as in (C).

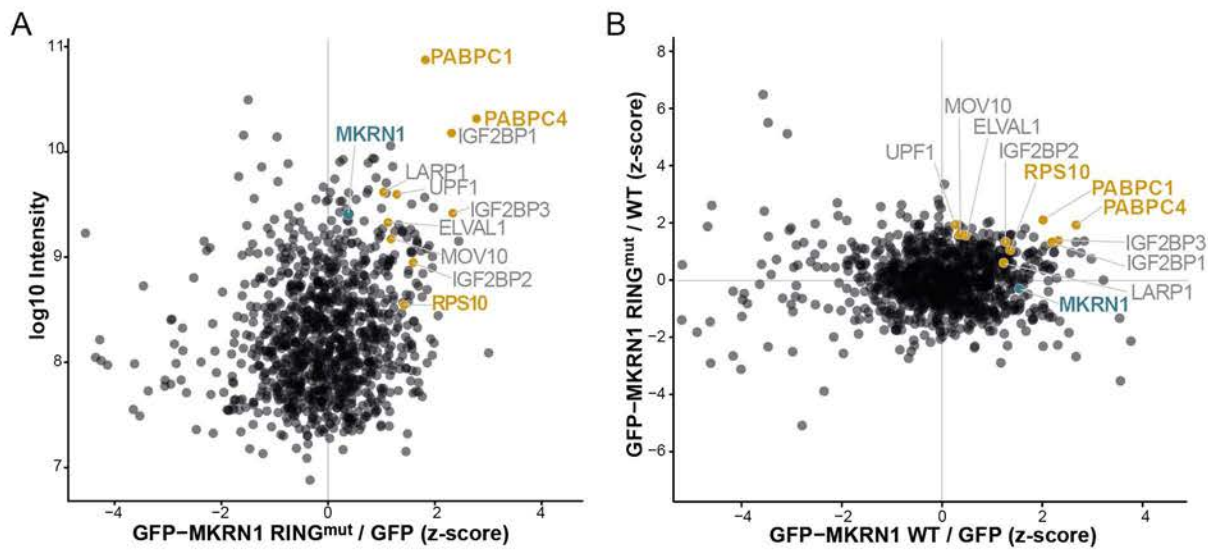


Supplemental Figure S4. MKRN1 binds upstream of long A-stretches. (A) The top 20% MKRN1 binding sites show a strong RNA binding preference for AAAA. Scatter plot compares the frequency of 4-mers within the 9-nt MKRN1 binding sites and flanking 40-nt windows for the top 20% and bottom 20% MKRN1 binding sites (according to SOB). 4-mer frequencies are displayed as z-scores based on background distribution from binding site permutations. (B) Heatmap representation of 1,412 non-overlapping A-stretches at MKRN1 binding sites, sorted by increasing length (8-30 nt). Only A's are coloured. (C) Binding sites with associated A-stretches show stronger MKRN1 binding. Boxplot compares the SOB values of MKRN1 binding sites in 3' UTRs with and without associated A-stretches. Number of binding sites indicated inside box. (D) MKRN1 binding site strength (signal-over-background, SOB) increases with length of associated A-stretch. Mean and standard deviation of MKRN1 binding sites associated with A-stretches of increasing length (x-axis). MKRN1 binding sites without associated A-stretches are shown for comparison on the left. Number of binding sites in each category indicated as bar chart above.

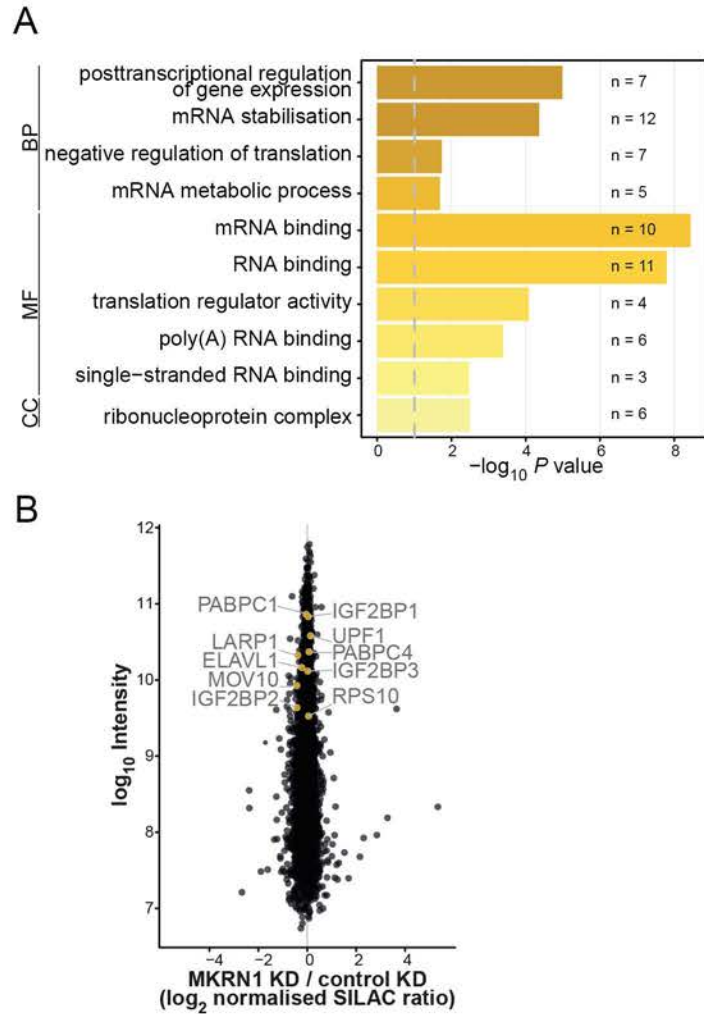


Supplemental Figure S5. Interaction with PABP is required for MKRN1 RNA binding. (A,B) UV crosslinking experiments to measure the RNA binding capacity of GFP-MKRN1^{wt} and GFP-MKRN1^{PAM2mut}. Autoradiographs (top) and Western blots (bottom) show GFP-MKRN1/RNA complexes and GFP-MKRN1 protein, respectively, in the eluates from replicates 2 (with 4SU and UV crosslinking at 365 nm) (A) and 3 (with conventional UV crosslinking at 254 nm) (B). For calibration, input samples for GFP-MKRN1^{wt} were diluted to 75%, 50% and 25% prior to GFP AP. Note that samples were loaded in different order in (B). Quantifications are given below. Uncropped gel images are shown in Supplemental Fig. S10.

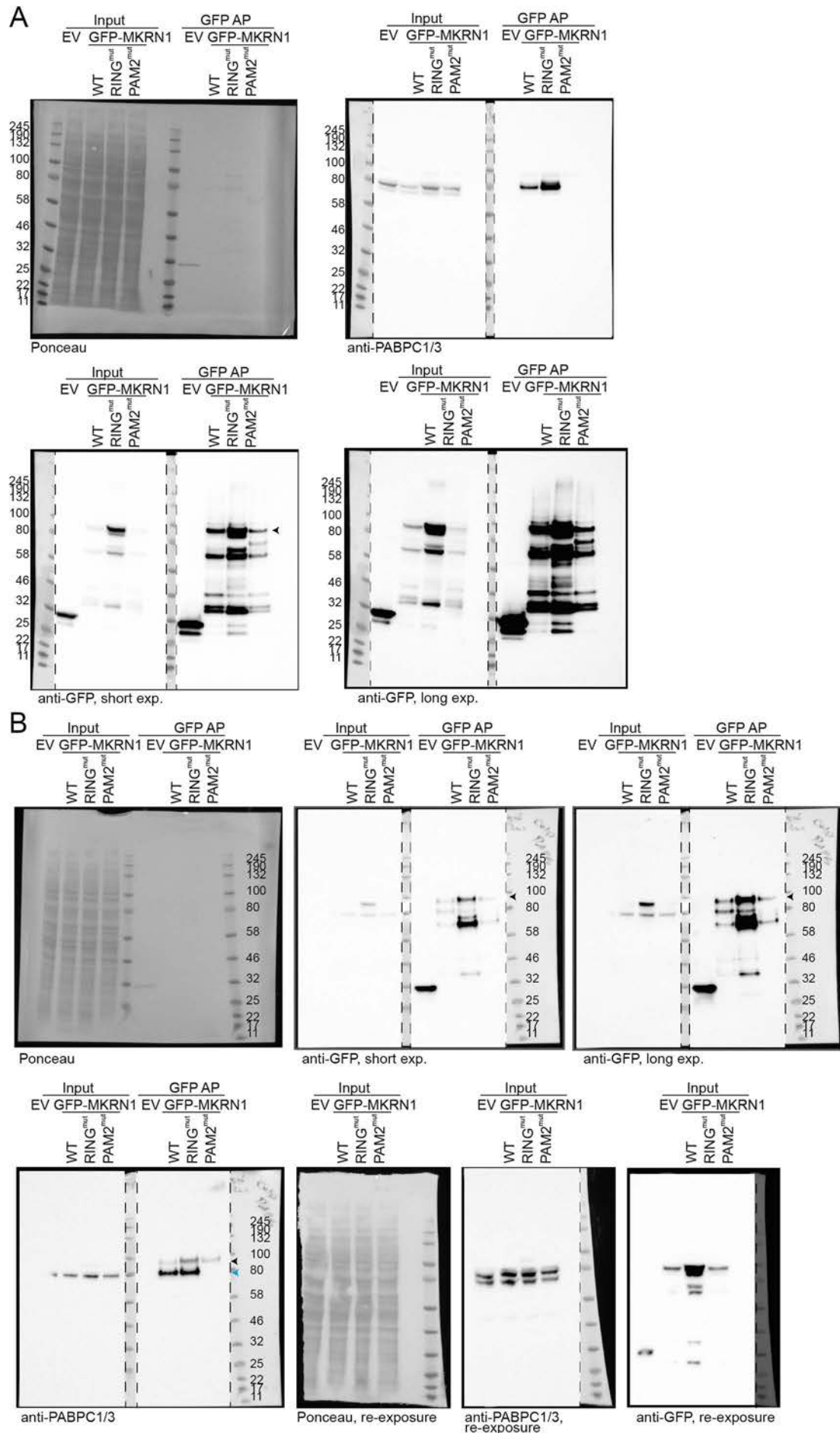
Supplemental Figure S6. MKRN1 is required to stall ribosomes at K(AAA)₂₀ in reporter assays. (A) Translation of dual fluorescence reporter plasmids was assessed by flow cytometry upon *MKRN1* and/or *ZNF598* KD. Median RFP:GFP ratios (normalised to K₀ in control KD) are shown for the reporter plasmids K₀, K(AAA)₁₂, K(AAA)₂₀, and R(CGA)₁₀. Error bars represent standard deviation of the mean (s.d.m., n ≥ 6 replicates; paired two-tailed t-test, Benjamini-Hochberg correction). Density plot of median RFP:GFP ratios of one replicate experiment with K(AAA)₂₀ with control or *MKRN1* KD (two independent siRNAs, KD1 and KD2) or *ZNF598* is shown on the right. (B) KDs of *MKRN1* and *ZNF598* were assessed by Western blot (n = 3 replicates). Black arrowhead indicates *ZNF598*. Replicates 2 and 3, and uncropped gel images are shown in Supplemental Fig. S11A,B. (C) *MKRN1* KD2 also reduces *MKRN2* levels. *MKRN1* KD1 and KD2 were performed for 72 h. Expression levels of *MKRN1* and *MKRN2* were assessed in relation to β -actin levels by qPCR in *MKRN1* KD (siRNA 1 and 2) and control KD. Error bars indicate s.d.m. (n = 2 replicates). (D,E) Cross-regulation of *MKRN1* and *ZNF598*. (D) *MKRN1* KD1 reduces endogenous *ZNF598* protein levels. Effect of *MKRN1* KD (KD1, siRNA 1 and KD2, siRNA 2) and *ZNF598* KD for 72 h was assessed by Western blot for endogenous *MKRN1* and *ZNF598*. Quantifications depict *MKRN1* or *ZNF598* expression levels in *MKRN1* or *ZNF598* KD over control KD condition, normalised to tubulin levels (n = 3 replicates). Replicates 2 and 3, and uncropped gel images are shown in Supplemental Fig. S11C,D. (E) *ZNF598* overexpression reduces *MKRN1* protein levels. Effect of *ZNF598* and *MKRN1* (wt and mutants) overexpression was tested after 48 h. Quantification as in (D). Uncropped gel images for all replicates are shown in Supplemental Fig. S11E,F.

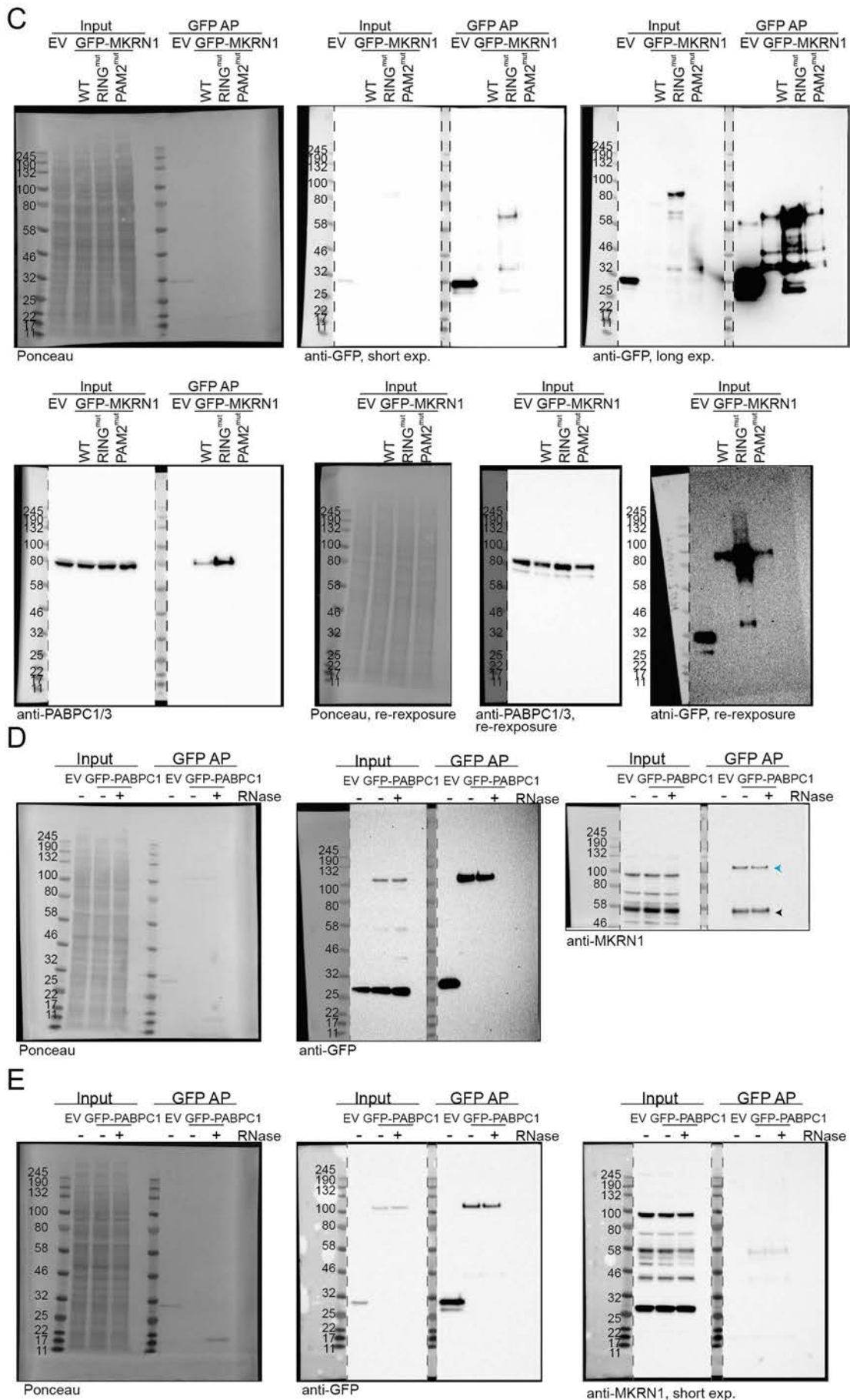


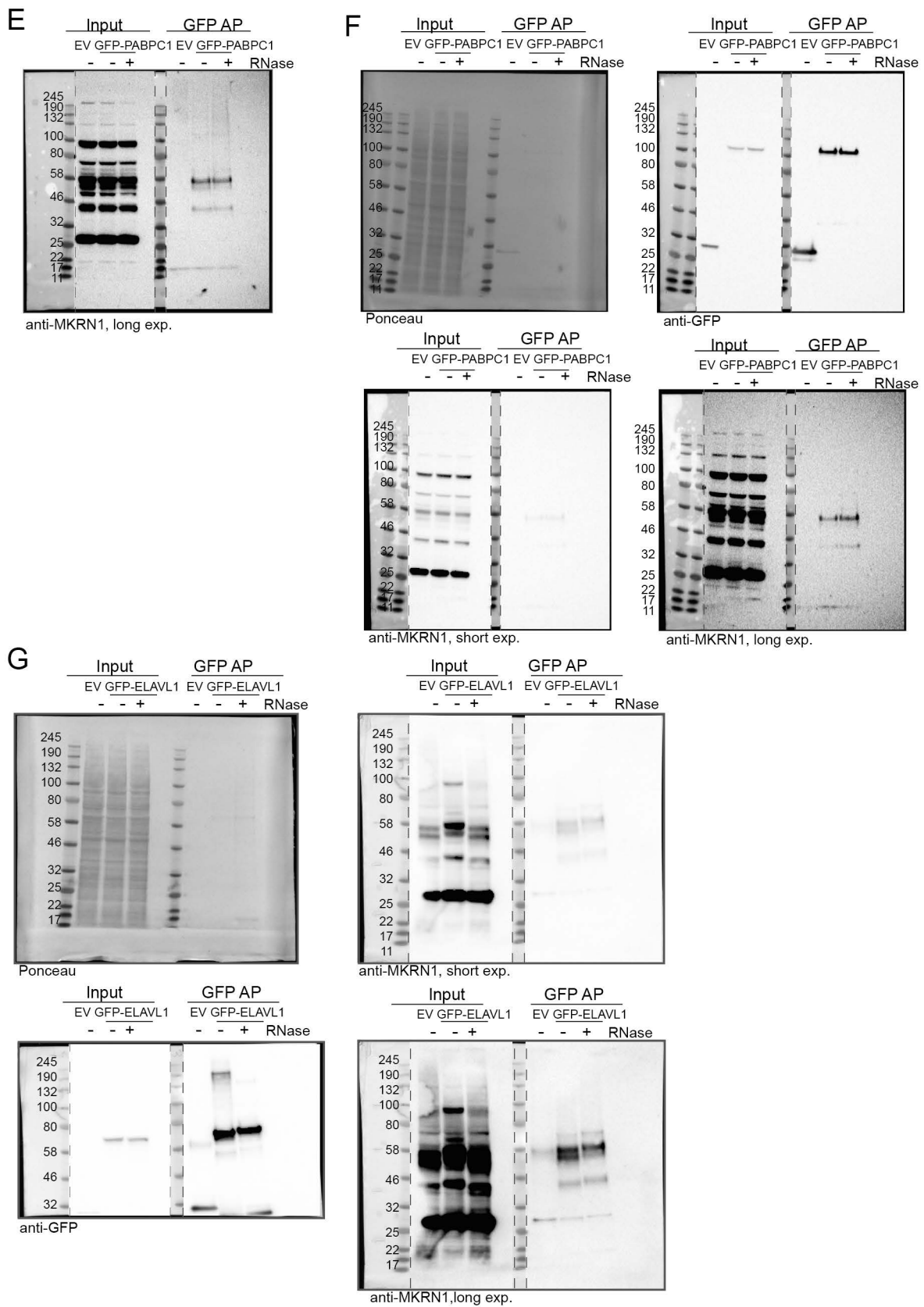
Supplemental Figure S7. Interactome of GFP-MKRN1^{RINGmut} reveals putative ubiquitylation substrates. Experiments were performed using SILAC-based MS. Asymmetrical z-scores of combined SILAC ratios ($n = 3$ replicates) are shown. Proteins are detected in at least two out of three replicates. (A) Protein interactome of GFP-MKRN1^{RINGmut} in HEK293T cells analysed by quantitative mass spectrometry. Combined SILAC ratios ($n = 3$ replicates) after z-score normalisation are plotted against \log_{10} -transformed intensities. 1,097 protein groups were quantified in at least two out of three replicates (Supplemental Table S1). MKRN1 and interesting candidate ubiquitylation targets are highlighted. (B) Quantitative comparison of the interactome of GFP-MKRN1^{wt} and GFP-MKRN1^{RINGmut} shows that potential ubiquitylation candidates identified in (A) are enriched in GFP-MKRN1^{RINGmut} over GFP-MKRN1^{wt}. Comparison reveals 137 proteins to be significantly enriched (GFP-MKRN1^{RINGmut} over GFP-MKRN1^{wt} with FDR < 5% and GFP-MKRN1^{wt}/GFP z-score > 1). Combined ratios of three replicates are shown in a scatter plot. Only proteins detected in at least two out of three replicates are shown. Highlighting as in (A).

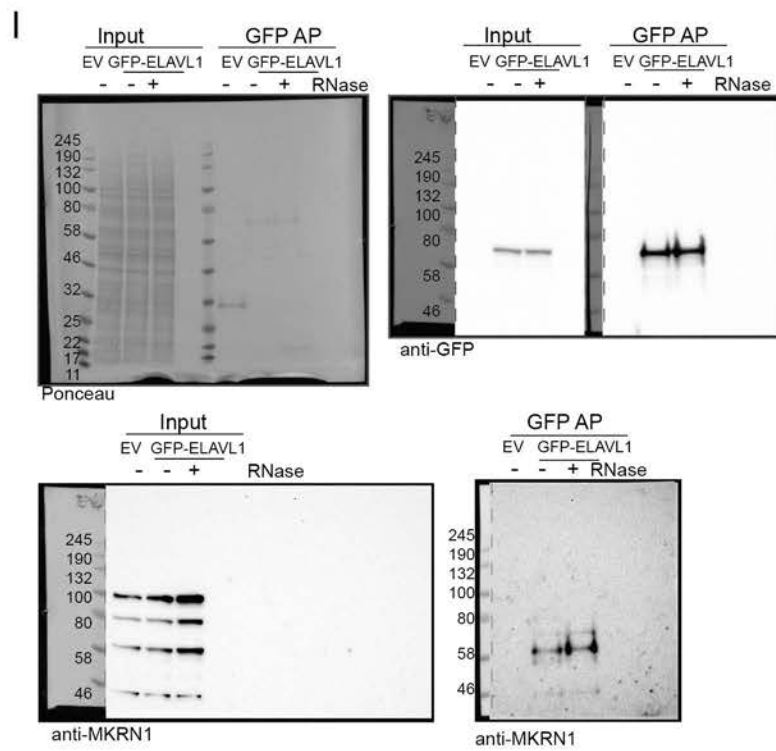
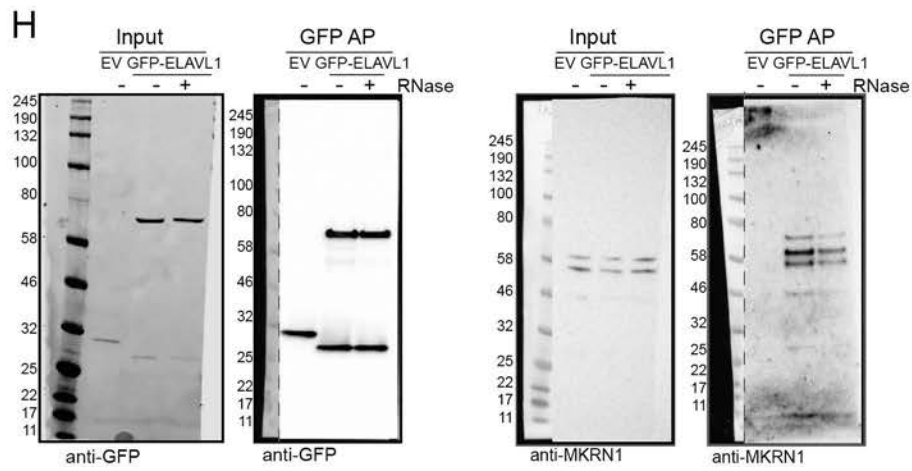


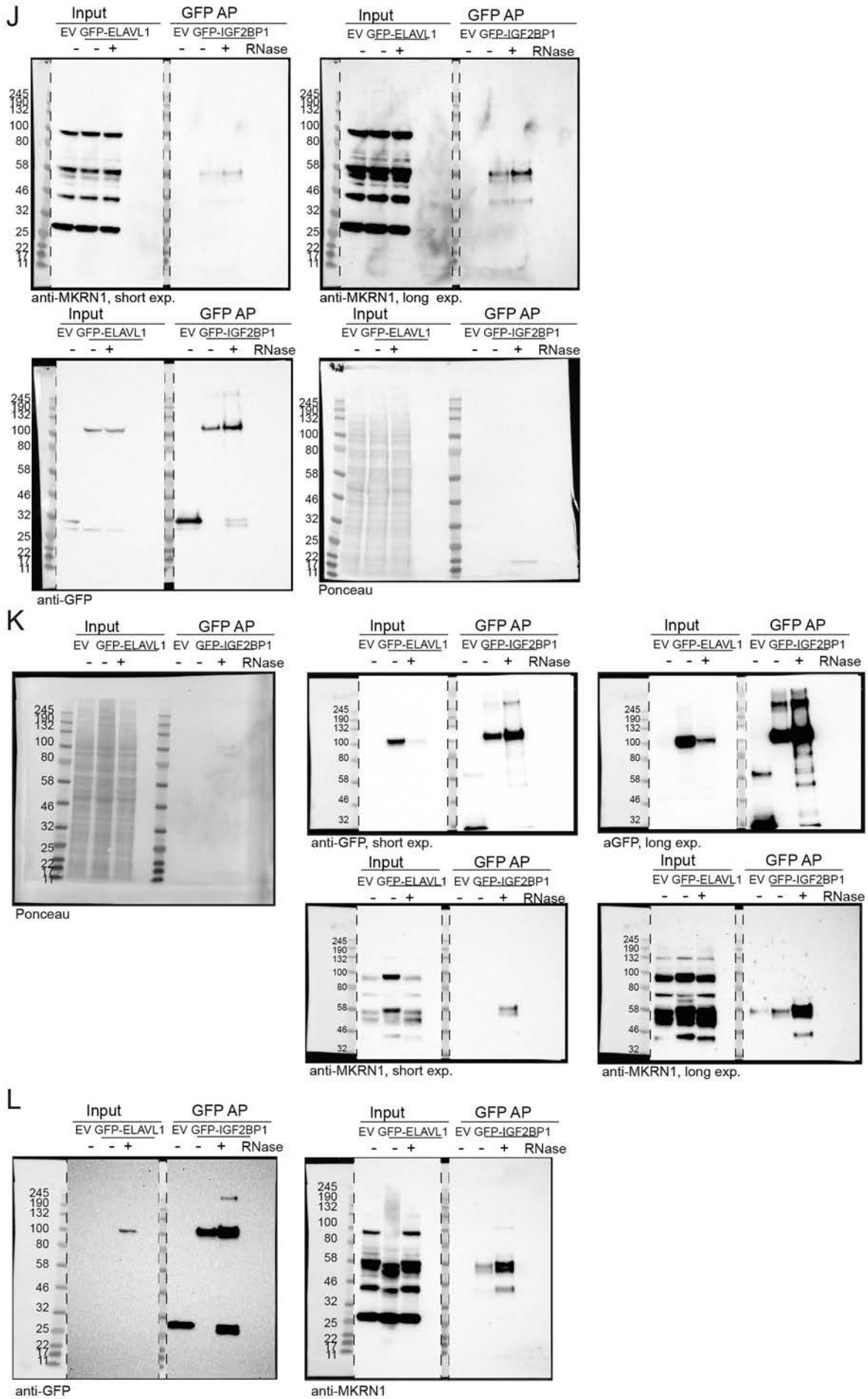
Supplemental Figure S8. GO term analysis of MKRN1 ubiquitylation targets and proteome analysis upon *MKRN1* KD. (A) GO terms enriched for the 21 MKRN1 ubiquitylation targets. Corrected *P* values (modified Fisher exact test, Benjamini-Hochberg correction) are depicted for all significant GO terms (corrected *P* value < 0.05) for Biological Process (BP), Molecular Function (MF) and Cellular Compartment (CC), together with the number of ubiquitylation targets associated with the respective term. (B) Proteome analysis of *MKRN1* KD in HEK293T cells analysed by quantitative mass spectrometry. Log₂-transformed, combined normalised SILAC ratios (*n* = 3 replicates) are plotted against log₁₀-transformed intensities. 6,425 protein groups were quantified in at least one out of three replicate experiments. Selected ubiquitylation targets of MKRN1 are highlighted.



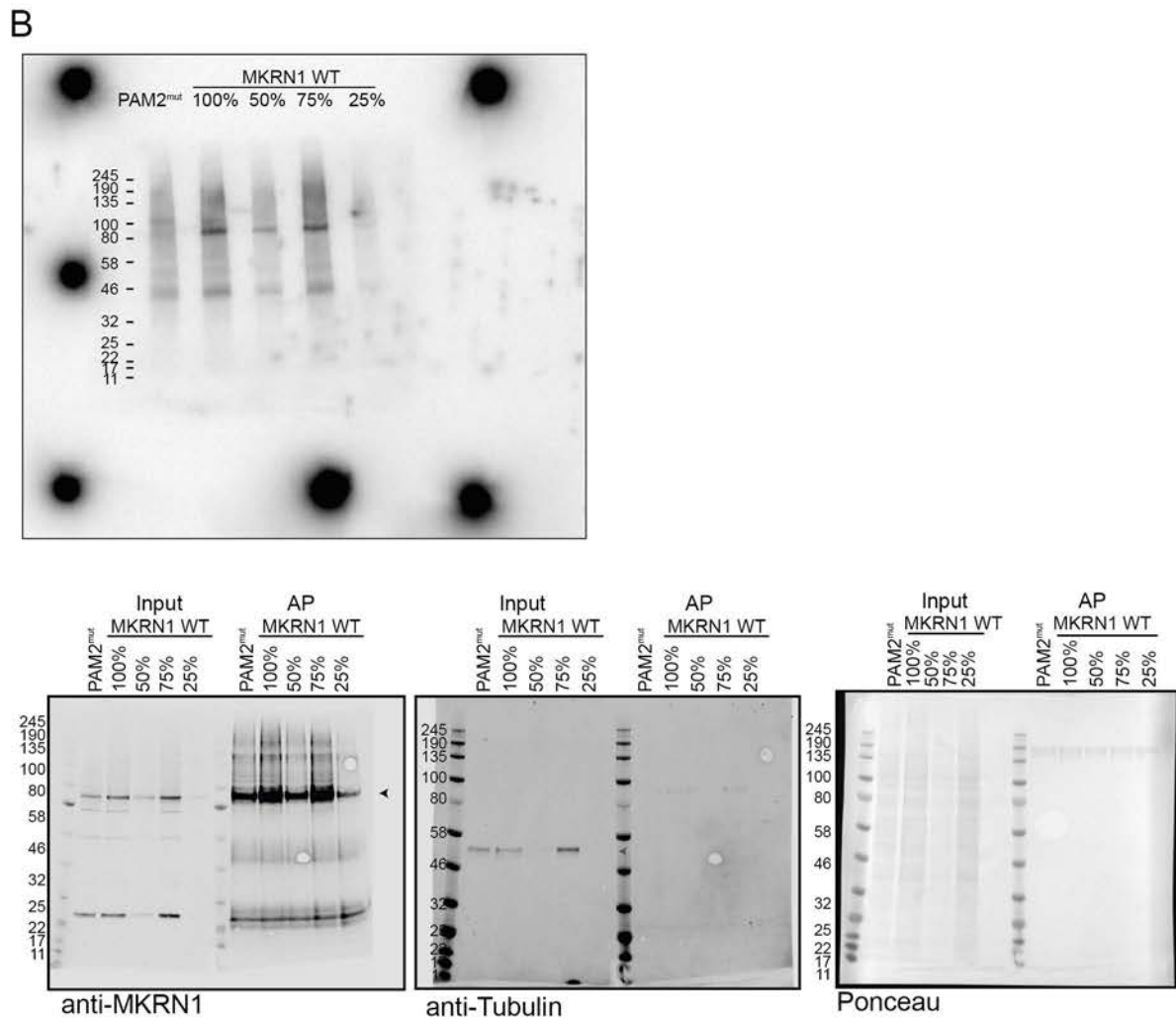
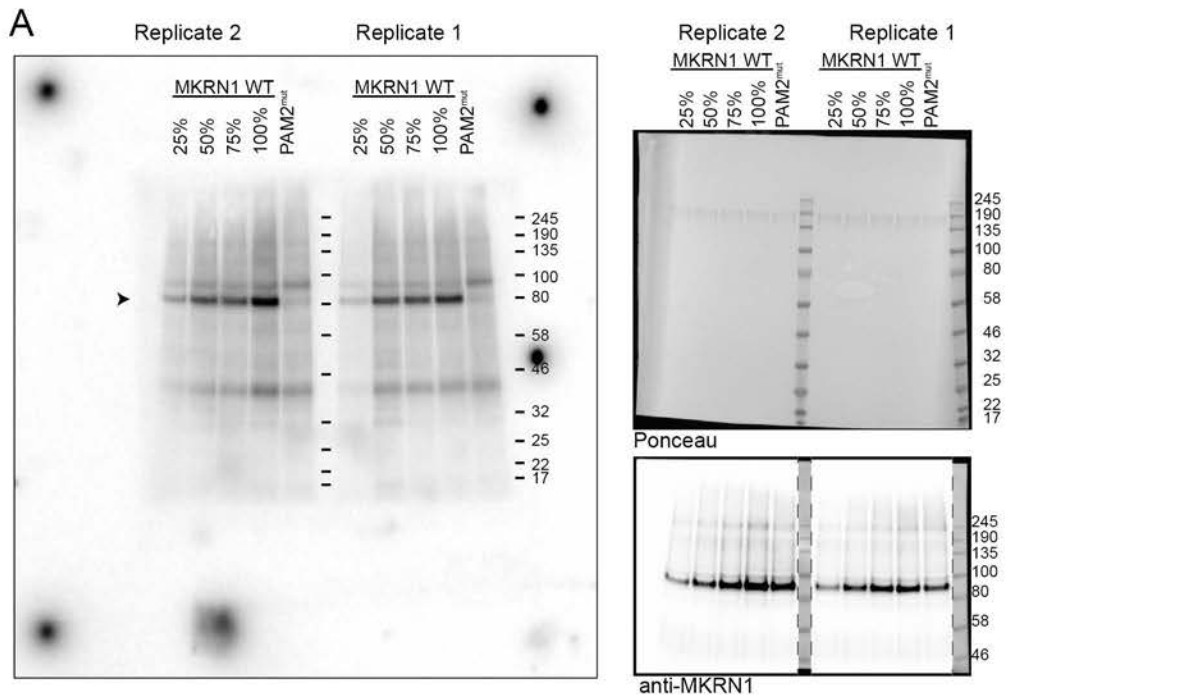






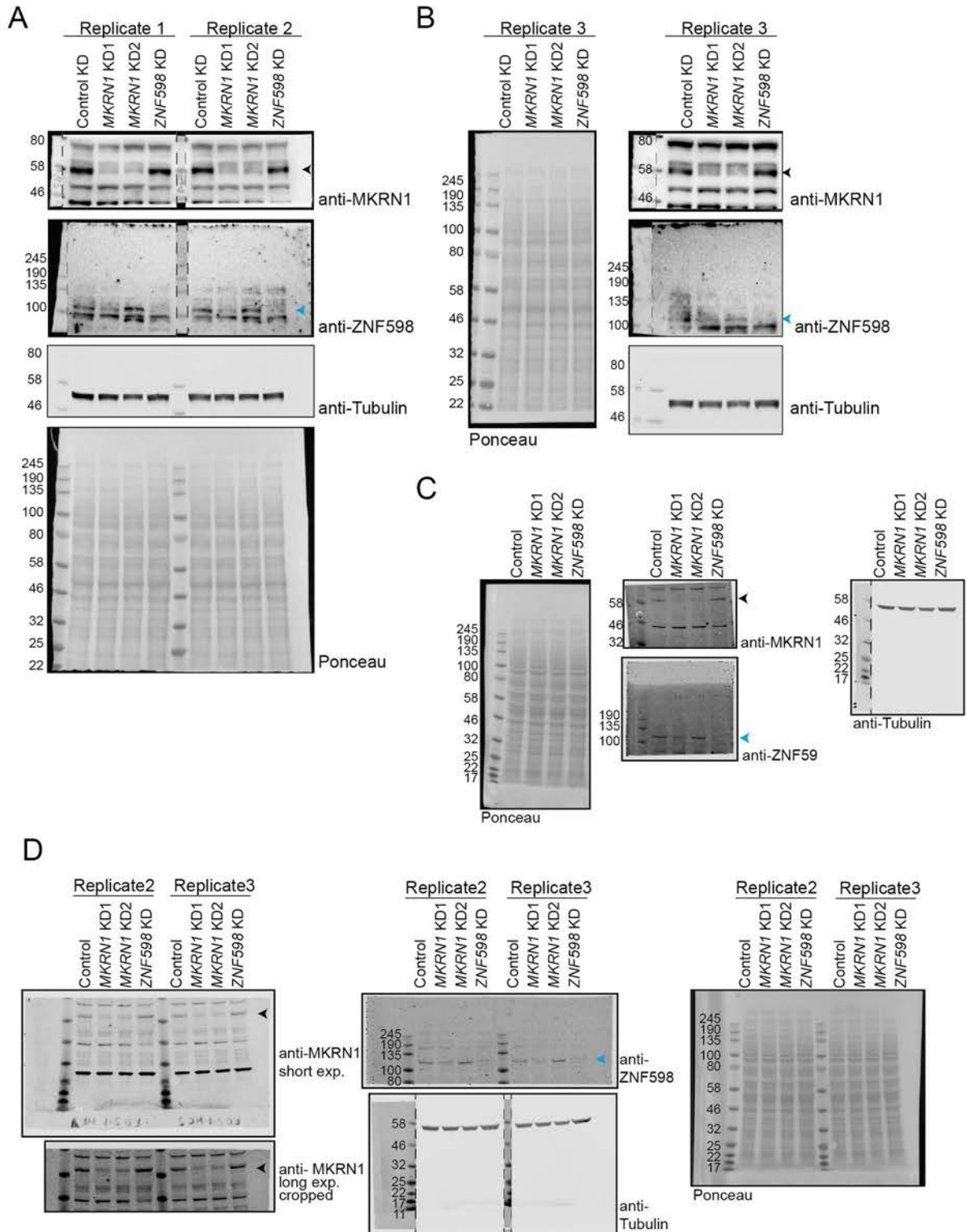


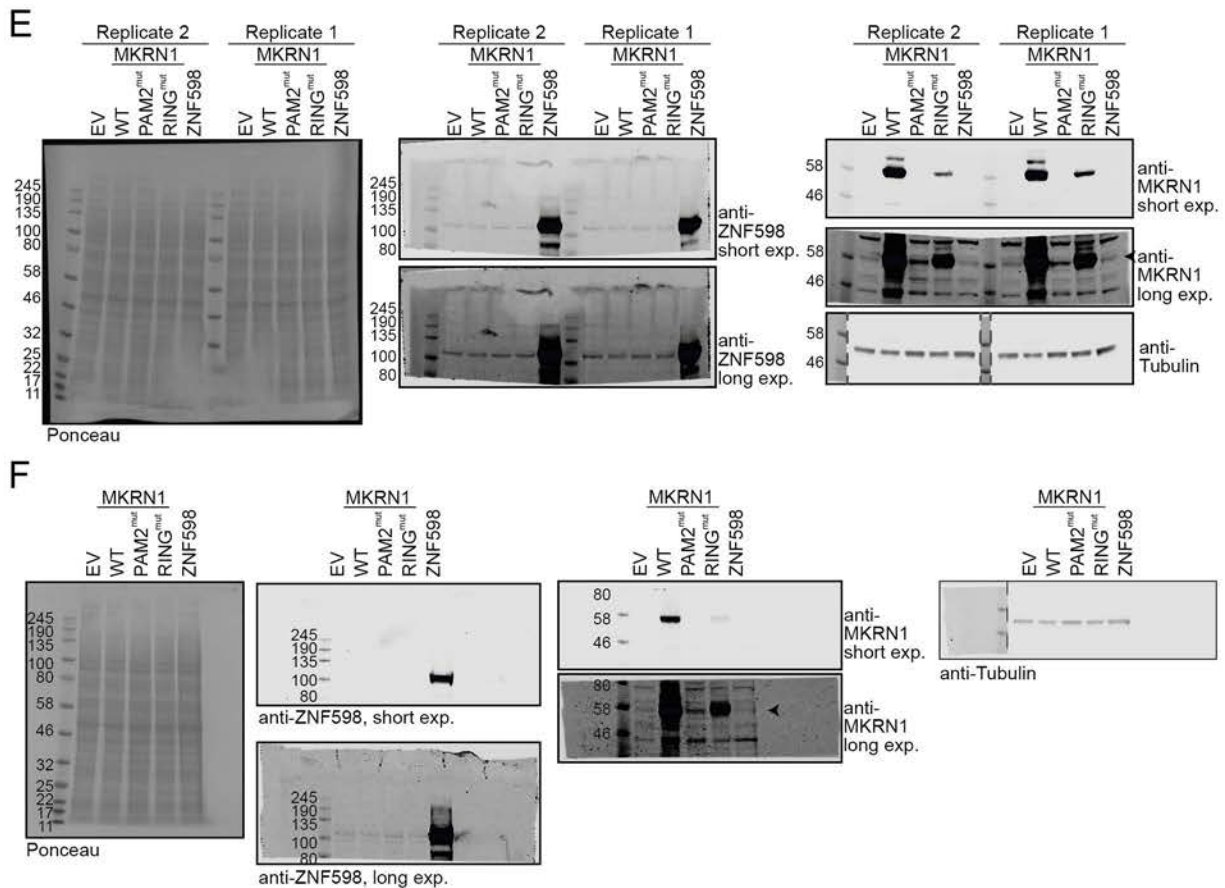
Supplemental Figure S9. Images of full membranes and different exposure times (exp.) for Western blot analyses in Fig. 1C and Supplemental Fig. S2C in the presence or absence of RNase A and T1. (A-C) PABP interacts with MKRN1^{wt} and MKRN1^{RINGmut} but not MKRN1^{PAM2mut}. Western blot analysis was performed with antibodies against PABPC1/3 and GFP. Images of full membranes and different exposure (exp.) times for both antibodies are shown for replicate 1 (A) which is presented in Fig. 1C, as well as replicates 2 (B) and 3 (C). Black and blue arrowheads indicate GFP-MKRN1 and PABPC1/3, respectively. (D-F) Endogenous MKRN1 interacts with GFP-PABPC1 independent of RNA. Western blot analysis was performed with antibodies against MKRN1 and GFP. Images of full membranes and different exposure times for both antibodies are shown for replicate 1 (D) which is presented in Supplemental Fig. S2C, as well as replicates 2 (E) and 3 (F). Black and blue arrowheads indicate MKRN1 and GFP-PABPC1, replicates. (G-I) Endogenous MKRN1 interacts with GFP-ELAVL1 independent of RNA. Western blot analysis was performed with antibodies against MKRN1 and GFP. Images of full membranes and different exposure times for both antibodies are shown for replicate 1 (G) which is presented in Supplemental Fig. S2C, as well as replicates 2 (H) and 3 (I). (J-L) Endogenous MKRN1 interacts with GFP-IGF2BP1 independent of RNA. Western blot analysis was performed with antibodies against MKRN1 and GFP. Images of full membranes and different exposure times for both antibodies are shown for replicate 1 (J) which is presented in Supplemental Fig. S2C, as well as replicates 2 (K) and 3 (L).



Hildebrandt_Supplemental_FigS10

Supplemental Figure S10. Images of full membranes of autoradiographs and Western blot analyses in Fig. 3D (replicate 1) and Supplemental Fig. S5 (replicates 2 and 3). UV crosslinking experiments to measure the RNA binding capacity of GFP-MKRN1^{wt} and GFP-MKRN1^{PAM2mut}. Autoradiographs (A, left; B, top) and Western blots (A, right; B, bottom) show GFP-MKRN1/RNA complexes and GFP-MKRN1 protein, respectively, in the eluates from replicates 1 and 2 (with 4SU and UV crosslinking at 365 nm) (A) and 3 (with conventional UV crosslinking at 254 nm) (B). (B) Images of full membranes of Western blot analyses with both antibodies are shown for replicate 3 (B).





Supplemental Figure S11. Images of full membranes and different exposure (exp.) times for Western blot analyses in Supplemental Fig. S6B,D,E. (A,B) KDs of *MKRN1* and *ZNF598* assessed by Western blot ($n = 3$ replicates) from Supplemental Fig. S6B. Western blot analysis was performed with antibodies against *MKRN1*, *ZNF598*, and tubulin. Black and blue arrowheads indicate *MKRN1* (53 kDa) and *ZNF598* (99 kDa), respectively. Uncropped gel images of replicates 1 and 2 (A) and 3 (B). (C,D) Images of full membranes are shown for cross-regulation between *MKRN1* and *ZNF598* KD from Supplemental Fig. S6D. *MKRN1* KD1 reduces endogenous *ZNF598* protein levels. Western blot analysis was performed with antibodies against *MKRN1*, *ZNF598*, and tubulin. Coloured arrowheads as in (A). Uncropped gel images of replicate 1 (C) and replicates 2 and 3 (D). (E,F) Images of full membranes are shown for cross-regulation of *MKRN1* and *ZNF598* overexpression (OE) from Supplemental Fig. S6E. *ZNF598* OE reduces *MKRN1* protein levels. Western blot analysis was performed with antibodies against *MKRN1*, *ZNF598*, and tubulin. Black arrowheads indicate *MKRN1*. Images of full membranes and different exposure times (exp.) for both antibodies are shown for replicates 1, 2 (E), and 3 (F). Note the opposite order of replicates 1 and 2 (2 left, 1 right) in (E).